RICE UNIVERSITY

Size-Controlled Synthesis of Monodispersed Gold Nanoparticles via Carbon Monoxide Reduction

by

Joseph Keith Young

A THESIS SUBMITTED
IN PARTIAL FULFILLMENT OF THE
REQUIREMENTS FOR THE DEGREE

Master of Science

APPROVED, THESIS COMMITTEE:

Rebekah Drezek, Chair
Professor of Bioengineering
Professor of Electrical and Computer Engineering

Junichiro Kono
Professor of Electrical and Computer Engineering

Kevin Kelly
Associate Professor of Electrical and Computer Engineering

Illya V. Hicks
Associate Professor of Computational and Applied Mathematics

HOUSTON, TEXAS
April 2011

ABSTRACT

Size-Controlled Synthesis of Monodispersed Gold Nanoparticles via Carbon Monoxide Reduction

by

Joseph K. Young

In this thesis an in depth analysis of nanoparticle synthesis utilizing carbon monoxide as a reducing agent is presented. Synthesized nanoparticle mono and polydispersity was examined via particle distribution profiles, statistical, and spectral analysis and compared against other reduction methods. The size and monodispersity of the gold nanoparticles produced with carbon monoxide were tunable by altering the concentration of $HAuCl_4$ and gas injection flow rates. The carbon monoxide based reduction method offered excellent tunability over a broad range of sizes while maintaining a high level of monodispersity when compared to the other reduction methods. The mechanisms involved in the size dependent optical response of the synthesized nanoparticles were identified. It was also found that speciation of aqueous $HAuCl_4$ influences the size, structure, and properties of Au colloids. Ensemble extinction spectra and TEM images provide clear evidence that CO reduction offers a high level of tunability compared to other synthesis methods.

Acknowledgements

First and foremost I would like to acknowledge God who is my strength and without God nothing I have accomplished would have been possible. I thank God for giving me the knowledge, vision, and ability to carry out my research. I would like to thank my mother, Amina, for sacrificing so much to ensure her children were provided for and for all the encouragement she has given me over the years. Her love for me, and her support of my academic pursuits, were intrinsic to my wanting to pursue a graduate education. I would like to thank Martha Alexander who is like a second mother and a true friend.

I would like to thank my advisor Dr. Rebekah Drezek for preparing me to be the best in my field and helping me excel. I would especially like to thank Dr. Drezek for allowing me to join her research group. The opportunity afforded me, since joining her lab, has been extraordinary. Her dedication to the welfare of her lab continues to amaze me and it has been a true blessing to be a member of her lab. I would like to thank my co-advisor Dr. Illya Hicks for his support and encouragement. He has continued to emphasize the importance of academic excellence and graduate education. I would like to thank my co-advisor Dr. Junichiro Kono for his continued support of my graduate education and for his willingness to serve on my committee. I would like to thank Dr. Kevin Kelly for his encouragement and willingness to serve on my committee. He has always presented himself as someone willing to listen and offer advice.

I would like to thank all the members of the Drezek lab for creating such an encouraging environment to work in. I would like to thank my close friends Cyre Kalu, Chrishonda Crawford, Travis McPhail, and Felicia Beal for their prayers and support.

TABLE OF CONTENTS

List of Figures

Chapter 1: Introduction

Nanoparticles are of immense scientific importance as they are in effect a link amid bulk materials and atomic or molecular makeup. A bulk material ought to encompass continuous physical properties in spite of its size; however, at the nano-scale size-dependent properties are often observed. Consequently, the properties of materials amend when their dimension approaches the nanoscale and as the proportion of atoms at the exterior of a material becomes considerable. For bulk materials larger than one micron, the percentage of atoms at the surface is immaterial in comparison to the quantity of atoms in the bulk of the material. The fascinating and sometimes unforeseen properties of nanoparticles are consequently largely due to the large surface area of the material, which governs the contributions made by the small bulk of the material. Metallic nanoparticles have attracted substantial attention due to their distinctive properties and various applications.

Gold nanoparticles possess optical and electrical properties that are distinct from those of the bulk phase. Gold nanoparticle colloidal solutions show a very intense color, which is lacking in the bulk material in addition to the individual atoms. The origin of this phenomenon is attributed to the fact that gold nanoparticles can exhibit a strong optical response due to the excitation of surface plasmons by an interacting electromagnetic field. Surface plasmon resonance (SPR) or localized surface plasmon resonance (LSPR), for nanometer metallic structures, is the collective oscillation of the conduction electrons of a metal. The plasmon derived optical resonance of gold nanoparticles is dependent on a variety of factors, such as the relative dimensions of the

nanoparticles, interparticle interactions, and their dielectric environment. By simply adjusting the size of the gold nanoparticles this optical resonance can be positioned over hundreds of nanometers in wavelength across the visible into the near infrared spectrum [5, 10].

These features render gold nanoparticles useful for many applications such as biophotonics, diagnostics, and conducting polymers [1, 19, 29-30]. In particular gold nanoparticles were investigated with regard to potential applications in optics, catalysts, and biology [16-20]. Many researchers have also exploited the biomedical applications of gold nanoparticles for thermal ablative cancer therapy, immunoassays, and gene therapy [16, 30]. Since the strong optical response is due to the excitation of surface plasmons and since these oscillations are on the boundary of the metal and the external medium, these waves are very sensitive to any change of this boundary, such as the adsorption of molecules to the metal surface. As a result of possessing this high surface sensitivity, for example, gold nanoparticles have garnered significant interest for the application of surface enhanced Raman scattering (SERS) leading to advantages in trace biodetection [7]. Surface enhanced Raman scattering is a surface sensitive technique that results in the enhancement of Raman scattering by molecules adsorbed on rough metal surfaces. The enhancement factor can be as much as 10^{14} -10^{15}, which allows the technique to be sensitive enough to detect single molecules. These gold nanoparticles can act as building blocks paving the way for fabricating biological labels, biological sensors, bioanalysis and biodiagnosis technologies, environmental detection of biological reagents, and even medical clinical diagnosis and therapy [31-33].

Chapter 2: Au Nanoparticles

2.1 Au nanoparticle reduction methods

Since the plasmon derived optical resonance of gold nanoparticles is strongly related to the dimensions of the nanoparticles and morphology the ability to synthesize monodispersed gold nanoparticles is essential. Tunability is also important since certain optical responses can, relating to AuNP size, find use in different applications. The most popular and reliable method to produce gold nanoparticles uses the aqueous phase synthesis of gold nanoparticles, which depends on the reduction of tetrachloroauric acid in the presence of a reduction agent [2-9]. A plethora of different reducing agents can be used for the reduction of tetrachloroauric acid however these agents have a significant influence on the morphology of the final product, many of which lead to polydispersed nanoparticle solutions. To date, many methods have been established to synthesize AuNPs from about 1nm to several micrometers in diameter. A typical and widely used method is based on the reduction of tetrachloroaurate ions in water using sodium citrate as a reductant to obtain AuNPs with diameters ranging from 16 to 147nm [3, 5, 19]. This method has shown a good control over the particle size, but good monodispersity is limited to the synthesis of larger particles typically in the range of 25 to 120 nm. Smaller-size AuNPs (from 1 to 5 nm) are usually prepared by borohydride reduction in the presence of thiol capping ligands [29]. Disadvantages of this method include the use of a toxic organic solvent and the potential presence of impurities introduced by use of capping ligands which also hinder the surface modification and functionality of particles

for particular applications [1]. Gold nanoparticles have also been synthesized using formaldehyde as a reducing agent offering varying degrees of monodispersity. Even though there are well established methods for the fabrication of gold nanoparticles there has never been an in depth study of nanoparticle fabrication utilizing carbon monoxide as a reducing agent.

In this paper an in depth analysis of nanoparticle synthesis utilizing carbon monoxide gas as a reducing agent is presented. Gold nanoparticles were synthesized utilizing different reducing agents that consisted of sodium borohydride ($NaBH_4$), trisodium citrate ($Na_3C_6H_5O_7 \cdot 2H_2O$), formaldehyde ($H_2CO$) and carbon monoxide gas (CO). After synthesis gold nanoparticle mono and polydispersity was examined. The size and monodispersity of the gold nanoparticles were tunable by varying certain factors during the synthesis process. The CO reduction method offered excellent tunability over a broad range of sizes while maintaining a high level of monodispersity when compared to the other reduction methods. Ensemble extinction spectra and TEM images provide clear evidence that CO reduction offers a viable alternative to citrate based synthesis. Several steps were taken to implement the different procedures for the various reducing agents for the reduction of aqueous Au^3 to Au^0.

2.2 Characterization

Sample size distributions were determined by transmission electron microscopy (TEM) performed using a JEOL 1230 High Contrast Transmission Electron Microscope (HC-TEM) operating at between 80kV and 100kV. A Hitachi S-5500 scanning electron microscope was also employed in scanning transmission electron microscope (STEM)

mode under bright field. Samples were prepared for both instruments by contacting a 10uL drop with a carbon film coated 200 mesh copper grid. The grids were placed in a spotlessly clean container, covered and allowed to dry completely before use.

The optical response of the gold nanoparticles was determined by examining the optical extinction spectra of aqueous samples in 1cm path length polystyrene cuvettes that was collected using a Varian Cary 300 UV-Visible scanning spectrophotometer. The UV-visible spectra were acquired at wavelengths between 400 to 800nm. Distilled water was used as the reference and the blank for baseline subtraction.

To further confirm the formation of Au atoms from $HAuCl_4$ and determine elemental surface coverage X-ray photoelectron spectroscopy (XPS) was carried out using a PHI Quantera SXM system. The soft x-ray source consisted of aluminum with source energy of 1486.7eV. The take off angle was set at 45 degrees. The sample was prepared by dropping colloidal solution on precut silicon wafers. The samples were placed in a spotlessly clean container, covered and allowed to dry. The samples were concentrated before dropping to ensure complete surface coverage of the substrate target area.

Chapter 3: Carbon Monoxide Gas Injection and Solubility

3.1 Carbon monoxide gas

Since the CO gas is responsible for the reduction of Au^3 to Au^0 it is of the utmost importance to fully understand processes by which the gas is introduced to the solution and what mechanisms are involved in CO reduction. CO solubility during gas injection into flowing water is studied using mathematical models. The solubility is determined during the initial stages of injection and is found to play a very important role in gold nanoparticle synthesis and monodispersity in aqueous conditions. To understand how the gas-injection flow rate influences nucleation rates and particle growth dynamics it is important to understand the mechanisms involved in carbon monoxide dissolving in water. Two possibilities for carbon monoxide gas dissolving in water, interstice filling and aquation, are examined. Some general observations can be made about the solubility of gases in general but two points can illustrate the two most important, as it relates to carbon monoxide reduction. First the solubility of gas increases with increasing pressure and decreases with increasing temperature. Second the solubility of gas depends on polarity and van der Waal's chemical bonds of molecules.

3.2 Interstice filling

There are two assumptions being made regarding the injection of carbon monoxide into an aqueous solution of $HAuCl_4$. There exist interspaces in the aqueous $HAuCl_4$ solution

and the inlet flow of carbon monoxide is such that a large percentage can fill in the interspaces prior to nucleation [13]. Due to the polarity of carbon monoxide being less than water and there is an absence of hydrolysis the contribution of carbon monoxide to the solubility is appreciable. It is also assumed that the carbon monoxide gas in interspaces can be described by the equation of state.

The amount of carbon monoxide filling in the interspaces can be calculated by the equation of state and the effective interspaces in the $HAuCl_4$ solution. It is difficult to measure the effective interspace of water at various concentrations of $HAuCl_4$ so the concept of the interspace ratio is implemented. It is defined as a specific gas being allowed to have access to a certain amount of aqueous solution at a constant temperature, the volume occupied by the gas is called the effective interspace and the effective interspace ratio can be expressed as

$$\Phi_i = {}^{V_j}\!/_{V_s} \,, \tag{1}$$

where V_j is the volume of the effective interspace, and V_s of the solution. Helium is used as a reference for scaling of the maximum interspace ratio in water due to helium having the largest effective interspace amongst all of the gases [25-27]. Using helium solubility data a regression equation of maximum effective interspace ratio vs. temperature ^{0}C is obtained as

$$\Phi_m = 0.009696 + 3.163917 * 10^{-5}x - 1.257929 * 10^{-6}x^2 + 2.129631 * 10^{-8}x^3 \,. \tag{2}$$

For carbon monoxide, its effective interspace ratio can be given by a calibration of the molecular size

$$\Phi_{CO} = \alpha_{CO} * \Phi_m \quad , \tag{3}$$

where α_{CO} is the volume factor of the molecules of carbon monoxide, defined by the ratio of van der Waals' volume of helium to carbon monoxide, i.e.

$$\alpha_{CO} = {}^{b_{He}}/_{b_{CO}} \, . \tag{4}$$

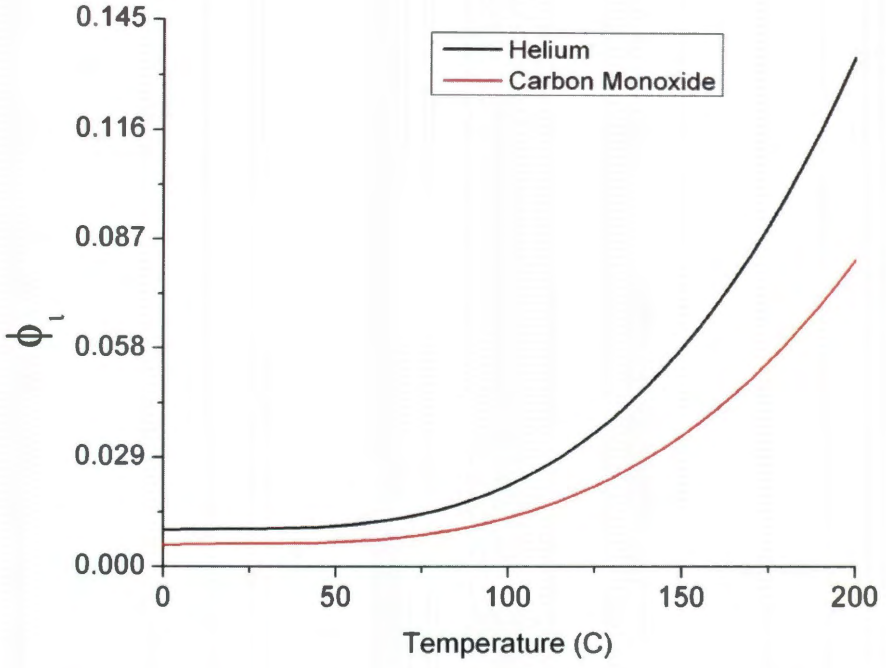

Figure 3.1. The effective interspace ratios for helium and carbon monoxide at different temperatures. Helium was used as a reference gas for the calculation of the effective interspace ratio for carbon monoxide.

The effective interspace ratios for helium and carbon monoxide at different temperatures, as shown in Figure 3.1 were calculated using the above equations. The solubility equations for gas filling in interspace can be formulated from the classical ideal gas law which is written as

$$pV = nRT \, , \tag{5}$$

and since the van de Waals' volume of carbon monoxide is determined by b_{CO} (m^3/mol), the equation of state can be rewritten as

$$P(V_j - n_j b_{CO}) = n_j RT \quad , \tag{6}$$

where n_j is the molar amount of gas in free state, and V_j is the effective interspace volume of the solution. Since

$$V_j = \Phi_{CO} * V_s \quad , \tag{7}$$

from equations (6) and (7), we have

$$n_j = \frac{pV_j}{RT + b_{CO}p} = \frac{p\Phi_{CO} * V_s}{RT + b_{CO}P} \ . \tag{8}$$

This equation is called the solubility equation of carbon monoxide filling in interspace.

3.3 Interactions as dissolving mechanism of carbon monoxide

During carbon monoxide injection into the aqueous $HAuCl_4$ solution some interaction could happen between the gas and the water. Suppose that during carbon monoxide injection into the solution temperature and pressure are kept constant and that the gas forms aquo complexes with water molecules. The chemical equilibrium is expressed as

$$CO(g) + nH_2O(l) = CO * nH_2O(l) + \Delta H \quad . \tag{9}$$

According to the principles of chemical equilibrium, it is clear that the amount of aquo complexes increases with lowering temperature and rising pressure. As the aquo complexes increase the solubility of the inlet gas as increases. To determine the number of aquo complexes it is first prudent to determine the number of water molecules available to form those complexes. In water-solute interactions the water molecules in the first layer around the solute differ from the bulk water [24-25].

According to Ahuir et al. there is a well known correlation between solubility and the number of water molecules in the first salvation shell. They determined that there are three surfaces that make up the van der Waals radius. These surfaces are van der Waals Surface (WS), Solvent Accessible Surface (SAS), and Solvent-Excluding Surface (SES).

First, the proper van der Waals surface, which is the external surface resulting from a set of spheres centered on the atoms or a group of atoms, forming the molecule. Second, the surface accessible to the solvent, defined as the surface generated by the center of the solvent, considered as a rigid sphere, when it rolls around the van der Waals surface. Third, the solvent excluding surface which was defined as being composed of two parts, the contact surface and the reentrant surface. The contact surface is the part of the van der Waals surface of each atom that is accessible to a probe sphere of a given radius. The reentrant surface is defined as the inward-facing part of the probe sphere when this is simultaneously in contact with more than one atom. SES is defined as the surface envelope of the volume excluded to the solvent, considered as a rigid sphere (probe sphere), when it rolls around the van der Waals surface [23]. The value of F_w was estimated by dividing the area of the Solvent Accessible Surface for carbon monoxide by the effective area occupied by a water molecule [23].

$$F_w = ASAS/(2r_w)^2 \quad . \tag{10}$$

The number of water molecules per carbon monoxide molecule is 17.2 and the number water molecules, per $HAuCl_4$ molecule, is 32.17.

If L_{H2O} represents the total number of H_2O molecules in a given volume, then L_{HAuCl4} represents the total number of $HAuCl_4$ molecules in a given solution. L_r is the remaining water molecules available to form aquo complexes with carbon monoxide and

$$N_h = \frac{L_{H2O} - L_{HAuCl4} * F_{HAuCl4}}{F_w} , \tag{11}$$

where N_h is the amount of CO-H2O aquo complexes. Suppose that a dissolving equilibrium of carbon monoxide gas is formed at a particular temperature and pressure. Since the concentration of water is far greater than that of gas, the equilibrium can be considered a constant. The equilibrium equation becomes

$$K_p = \frac{[CO * nH_2O]}{p} = \frac{N_h}{N_m * V_s * p} , \tag{12}$$

where N_m is Avogadro's constant and

$$N_h = N_m * V_s * p * K_p . \tag{13}$$

Thus the molar amount of dissolving gas in a certain amount of water is

$$n_h = \frac{N_h}{N_m} = V_w * p * K_p . \tag{14}$$

Here n_h shows the contribution of interaction dissolving mechanisms to the solubility of carbon monoxide in $HAuCl_4$ aqueous solution. Figure 3.2 shows the effect of increasing $HAuCl_4$ concentration on the number of available CO aquo complexes.

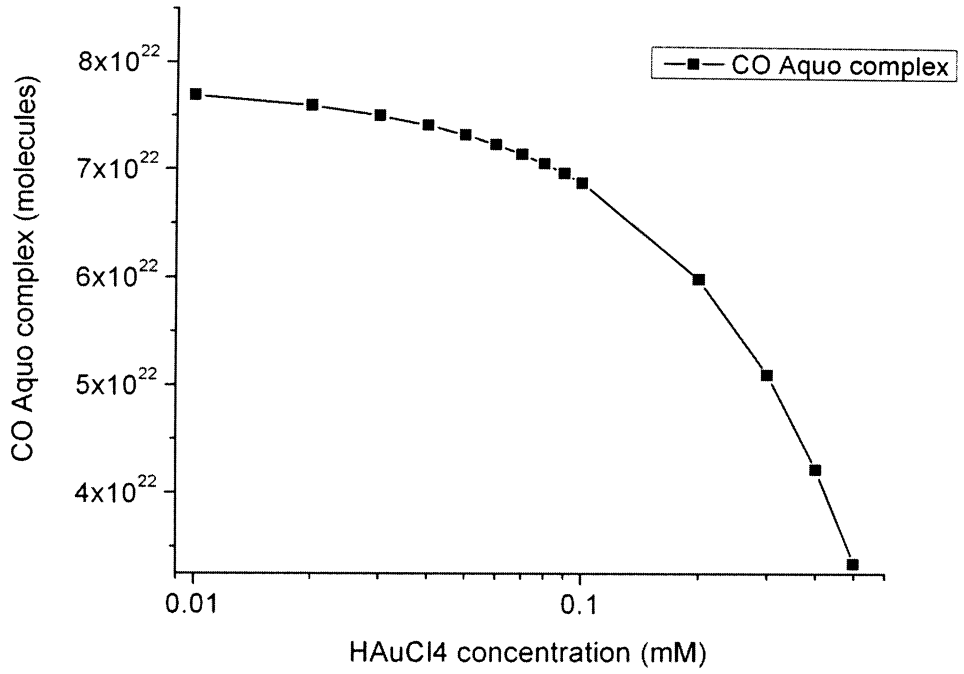

Figure 3.2. The amount of available aquo complexes as a function of increasing $HAuCl_4$ concentration.

3.4 The overall solubility of carbon monoxide gas

If the solutes in aquo complexes take up part of the interspace V_h, the remaining volume of interspace is V_{js}, and

$$V_{js} = V_j - V_h = \Phi_{CO} V_s - N_n b_{CO} \ . \tag{15}$$

Since the amount of free gas is related only with V_{js}, V_j in eq. (8) should be substituted with V_{js}, giving

$$n_j = \frac{pV_{js}}{RT + b_{CO}p} = \frac{p}{RT + b_{CO}P}(\Phi_{CO} V_s - N_n b_{CO}) \ . \tag{16}$$

From eqs. (14) and (16), the total amount of gas in water becomes

$$n = n_j + n_h = \frac{p}{RT + b_{CO}p}(\Phi_{CO} V_s - N_n b_{CO}) + V_s p K_p \ . \tag{17}$$

Introducing eq (13) into eq (17) and rearranging it gives

$$n = \mathrm{V_s}(\mathrm{pK_p} + \frac{p\Phi_{CO}}{RT + b_{CO}p} - \frac{b_{CO}p^2K_p}{RT + b_{CO}p}). \quad (18)$$

And the mole concentration of gas in unit volume becomes

$$c = \frac{\mathrm{n}}{\mathrm{V_s}} = \left(\mathrm{K_p} + \frac{\Phi_{CO}}{RT + b_{CO}p}\right)p - \frac{b_{CO}p^2K_p}{RT + b_{CO}p} . \quad (19)$$

In eq (19)m the units of p, b_{CO} and c are Pa, m^3 and $^{mol}/_{m^3}$, respectively. The solubility of gas is often expressed in the volume ratio of gas to water in normal state. So eq. (19) can be written as

$$\mathrm{R_s} = 0.0224\left[\left(\mathrm{K_p} + \frac{\Phi_{CO}}{RT + b_{CO}p}\right)p - \frac{b_{CO}p^2K_p}{RT + b_{CO}p}\right] . \quad (20)$$

Since the unit of solubility is expressed in unit mass of water, it is necessary that $\mathrm{R_s}$ should be divided by the density of the $HAuCl_4$ solution, yielding

$$\mathrm{R_m} = \frac{\mathrm{R_s}}{\mathrm{d}} \quad (^{\mathrm{mL}}/_{\mathrm{g}}) . \quad (21)$$

The density of water was accurately determined in previous investigations [27]. In order to calculate the density of the chloroauric solution we studied the relationship between the density of water, the density of $HAuCl_4$ at varying concentrations and temperature of the solution. We obtained regression equations for each of the varying molarities. The regression equation for a chloroauric solution at 20 degrees Celsius is

$$d_{20C} = -1.684149E-06x^4 + 6.046620E-05x^3 - 1.027943E-03x^2 + 2.629604E-03x + 1.000517 \quad (22)$$

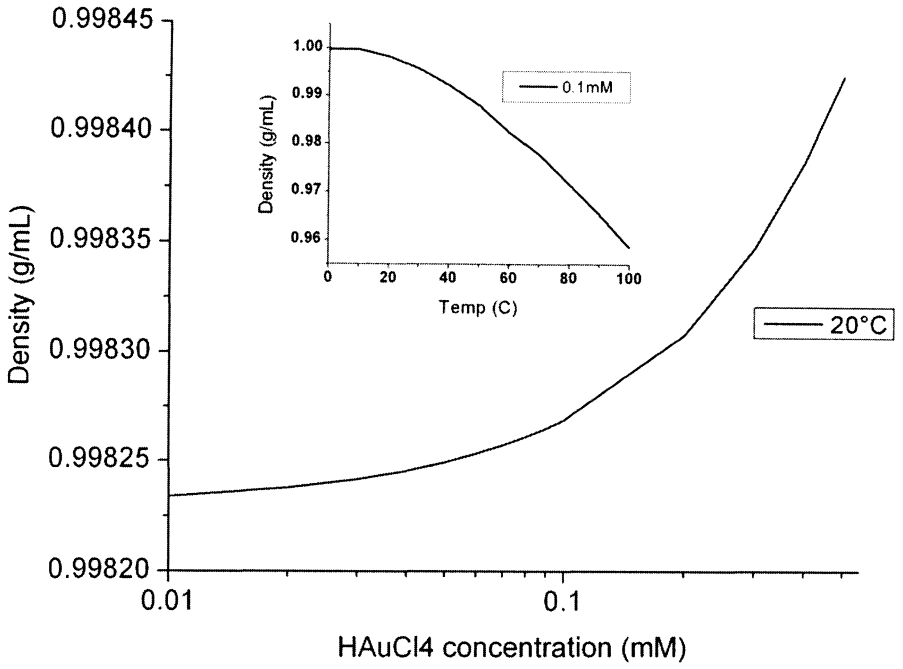

Figure 3.3. The density of the $HAuCl_4$ acid solution VS concentration at 20 degrees Celsius. The inset is $HAuCl_4$ solution density vs. temperature at a $HAuCl_4$ concentration of 0.1mM.

Figure 3.4 shows the contribution of both mechanisms to the solubility of carbon monoxide under a pressure of 1MPa in a $HAuCl_4$ acid solution with a concentration of 0.01mM and 0.09mM.

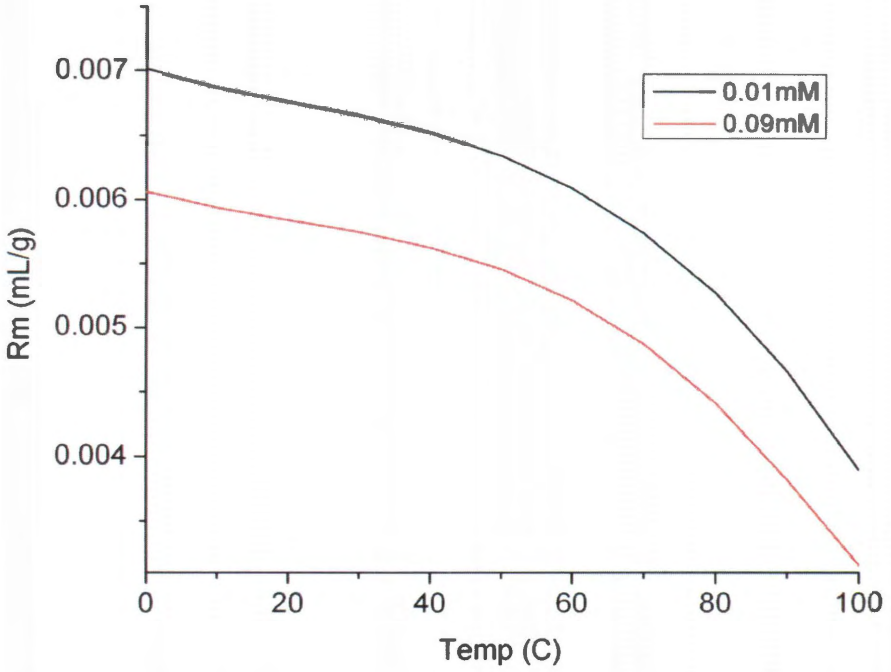

Figure 3.4. Contribution from two mechanisms to the overall solubility of carbon monoxide in a $HAuCl_4$ solution consisting on concentrations of 0.01mM and 0.09mM.

Chapter 4: Au Nanoparticle Synthesis

4.1 Pre-synthesis

Several chloroauric acid solutions were prepared for utilization with carbon monoxide reduction. Various weights of fresh chloroauric acid were dissolved in individual amber bottles containing 200mL of water. At least two separate batches of all solution concentrations were employed to confirm reproducibility. One set of solutions consisted of varying concentrations of $HAuCl_4$ ranging from .01mM up to 0.09mM in 0.01mM increments. Solutions ranging from 0.1mM to 0.9mM in .1mM increments and 1mM and 2mM solutions were prepared. 1% weight solution of $HAuCl_4$ was also prepared. All chloroauric acid solutions were aged in individual amber bottles under 4^0C and light protected for a minimum of three days prior to use. All trisodium citrate and hydrogen borohydride solutions were freshly prepared before use. All glassware used in the following procedures were cleaned in a bath of freshly prepared aqua regia solution (3 parts HCL acid to 1 part HNO_3) and rinsed thoroughly with ethanol three times and then rigorously rinsed four times with copious amounts of pure grade water and oven dried prior to use. Solutions were admitted by pipetters and each pipette tip was only employed for one specific reagent to avoid cross contamination. Stirring was conducted by a PTFE-coated magnetic stir bar that was cleaned and dried in the same manner as the glassware.

4.2 Synthesis of Au colloid using carbon monoxide gas

When the carbon monoxide is introduced into the aqueous $HAuCl_4$ solution electrons are donated to the $[AuCl_4]^-$ ions. For $[AuCl_4]^-$ ions to be reduced to gold atoms a series of redox reactions takes place which includes the liberation of Cl^- ions and is described below.

$$AuCl_4^- + 2e^- \rightarrow AuCl_2^- + 2Cl^- \quad (23)$$

$$AuCl_2^- + e^- \rightarrow Au^0 + 2Cl^-$$

The electrons are contributed from the reaction of carbon monoxide and dihydrogen monoxide and the reducing half reactions are as follows

$$CO(g) + H_2O \rightarrow CO_2(aq) + 2e^- + 2H^+ \quad (24)$$

$$CO(g) + 2H_2O \rightarrow HCO_3^- + 2e^- + 3H^+$$

The thermodynamics of $HAuCl_4$ reduction in aqueous solutions using CO is presented in appendix B.

Gold nanoparticles, synthesized by CO reduction, with average diameter nanoparticles ranging from 4.5nm to 52nm are prepared as described below. A set of solutions consisting of varying concentrations of $HAuCl_4$ ranging from .01mM up to 0.09mM in 0.01mM increments were utilized. For each HAuCl4 concentration five 40mL samples were prepared. Each sample was aerated at different flow rates controlled by a control valve. The five solutions were exposed to CO gas at flow rates of 16.9, 25.45, 31.59, 37.0, and 42.9 ml/min respectively. The effect of stirring speed is examined and it is found that the revolutions per minute (rpm) by which the solution is stirred plays a role in particle size and morphology, however, for the following discussion it is assumed that the solution is constantly stirred at a rate of 500 rpm until noted otherwise. Additionally,

the effects of gas-injection flow rates, and injection hole diameters on nanoparticle monodispersity and reaction completion times are investigated. The solution temperature, prior to aeration, was maintained between 18 and 20 degrees C.

To illustrate the effects of gas flow injection rates a solution consisting of a low chloroauric concentration was utilized. 0.01mM was used as the minimum concentration due to detection limitations of the Cary 300 UV-visible. Spectra of the nanoparticles synthesized from a solution of $HAuCl_4$ acid at a concentration of 0.01mM is shown in Figure 4.1.

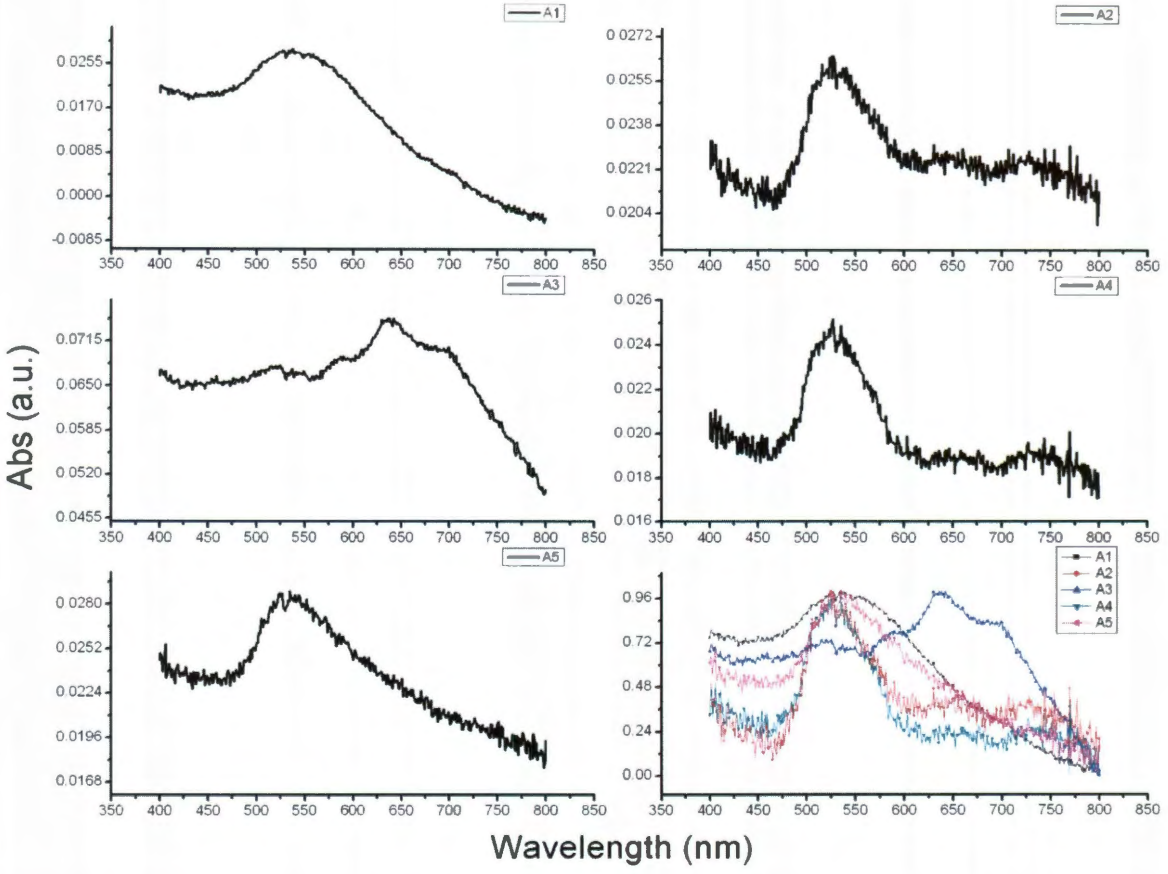

Figure 4.1. Samples A1 through A5 were aerated at flow rates of 16.9, 25.5, 31.6, 37.0, and 42.9 ml/min respectively. The spectrum at the bottom right is a normalized overlay of the five samples.

It can be seen that a smoother spectra was generated at the minimum flow rate of 16.9 mL/min when compared to the other injection flow rates. Even at this lower concentration the plasmon absorption is clearly visible. As the flow rate increases from 16.9 to 42.9 mL/min the change in spectral symmetry is clearly visible. TEM micrographs of the corresponding nanoparticles are displayed in Figure 4.2.

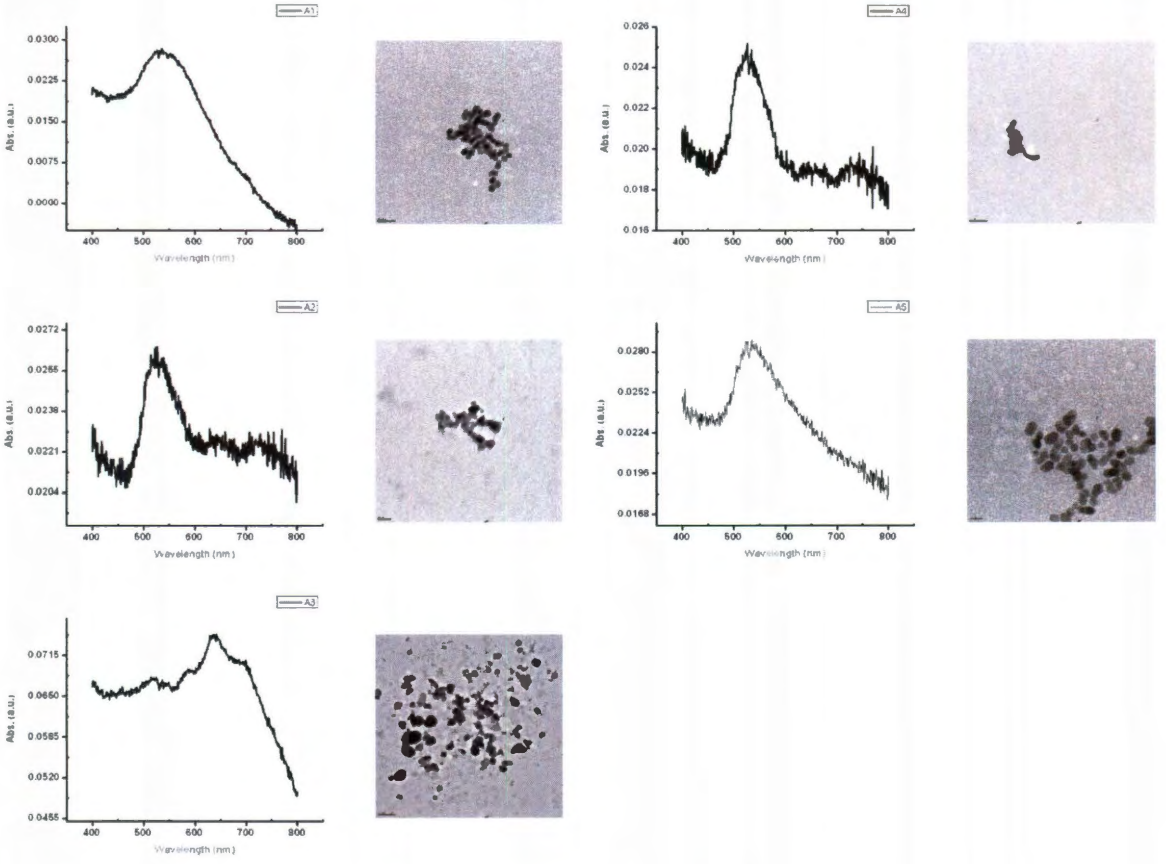

Figure 4.2. UV-visible extinction spectra with corresponding TEM micrographs.

The gas injection flow rate of 16.9 mL/min produced individual nanoparticles compared to the other injection flow rates. The nanoparticle sizes for A1 ranged from 5 to 11nm in diameter. Sample A2 possessed aggregates and irregularly shaped particulate matter

while sample A3 consisted of large particle masses and gold clumps ranging from 3nm to 2um in diameter. A CO flow rate of 37 mL/min (A4) resulted in fused particle chains. The TEM micrograph in sample A5 illustrates nanoparticle formation however the nanoparticles were elliptical in shape and very polydispersed. The nanoparticle sizes, in sample A5, ranged from 5 to 40nm in diameter. This size distribution is reflected in the broad plasmon band.

Increasing the chloroauric acid concentration reduced the polydispersity of the nanoparticles. Figure 4.3 shows the UV-visible spectra of nanoparticles synthesized from a chloroauric acid concentration of 0.3mM. As seen in the spectra of the 0.03mM sample a gas flow rate of 16.9 mL/min produced a very broad peak that narrowed as the flow rate increased towards 42.9 mL/min.

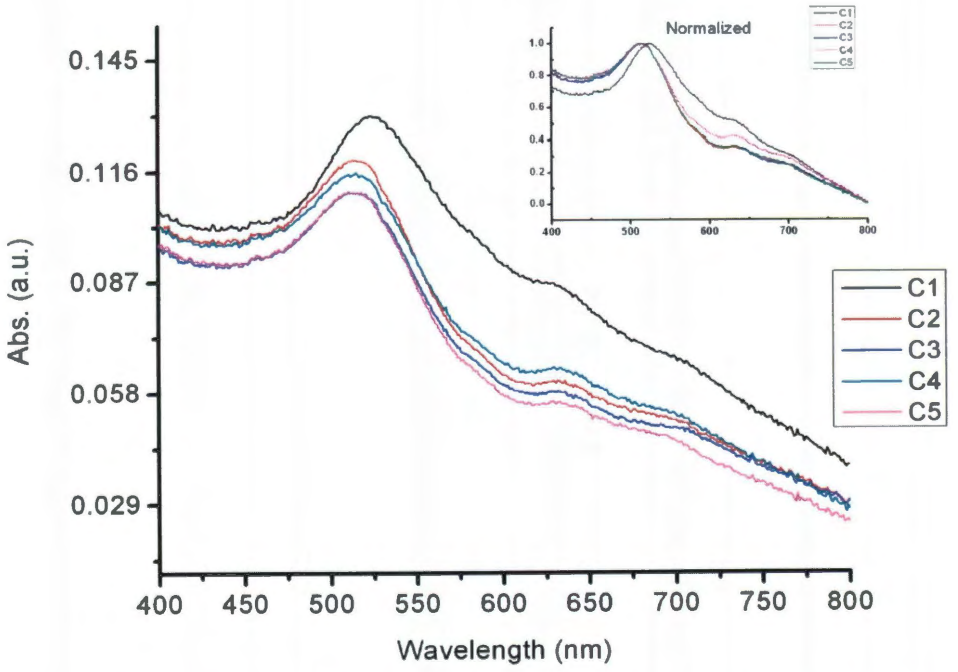

Figure 4.3. UV-visible spectrum of a 0.03mM $HAuCl_4$ sample aerated at 16.9, 25.5, 31.6, 37.0, and 42.9 ml/min corresponding to C1, C2, C3, C4, and C5 respectively. The inset is a normalized compilation of all five samples.

4.3 Au nanoparticle statistical analysis

Particle size distributions were obtained by examining the TEM micrographs and parameterized using WCIF ImageJ (Wright Cell Imaging Facility-Toronto Western Research Institute). ImageJ is a public domain Java image processing program inspired by NIH Image. The steps utilized to implement this program are shown in appendix A. The Toronto-Western Research Institute provided the nanoparticle parameter and analysis plugin. To ensure accuracy of the particle statistical analysis functionality of the program an additional parameterization mechanism was implemented. TEM images were parameterized by manually measuring a minimum of 100 particles per sample set to determine particle distributions. Only easily distinguishable particles were counted towards the particle size distribution. Overlapping nanoparticles or particle clusters that were not easily distinguishable, were not included in the size distribution. Images were parameterized according to $< d >$, the mean diameter from the measured diameter frequency distribution

$$< d > = \frac{\sum[n_i d_i]}{\sum[n_i]} ,$$

where $\sum$ is the sum on i over the whole sample, n_i is the number of particles within a certain small diameter range, and d_i the mean diameter of this range. For statistical analysis of the particles the standard deviation σ is determined. The standard deviation is the most common measure of variability, measuring the spread of the data set and the relationship of the mean to the rest of the data. If the data points are close to the mean, indicating that the responses are fairly uniform, then the standard deviation will be small. Conversely, if many data points are far from the mean, indicating that there is a wide

variance in the responses, the standard deviation will be large. The standard deviation is calculated using the following formula where σ is defined as

$$\sigma = \sqrt{\frac{1}{N-1}\sum_{i}^{N}(x_i - \bar{x})^2} \quad ,$$

where $\{x_1, x_2, x_3, \ldots, x_N\}$ is the sample and $\bar{x}$ is the mean of the sample.

Figure 4.4 shows the UV-visible spectra of nanoparticles synthesized from a chloroauric acid concentration of 0.3mM at flow rates of 16.9, 25.5, and 37.0 mL/min corresponding to samples C1, C2, and C4 respectively with accompanying TEM micrographs and histograms. The polydispersity of sample C1 is represented by a broad particle distribution curve. The particle sizes for C1 ranged from 2.5 to 17nm in diameter. Increasing the CO flow reduced the width of the particle distribution curve where an optimum inlet gas flow was obtained at 25.5 mL/min (C2). The mean standard deviation for sample C2 was 7%. Well below the 13 to 15% normally obtained for comparable sizes via citrate reduction. As the gas flow inlet rate increased the particle distribution curve widened. These results indicate that carbon monoxide inlet gas flow rates effects particle formation and monodispersity.

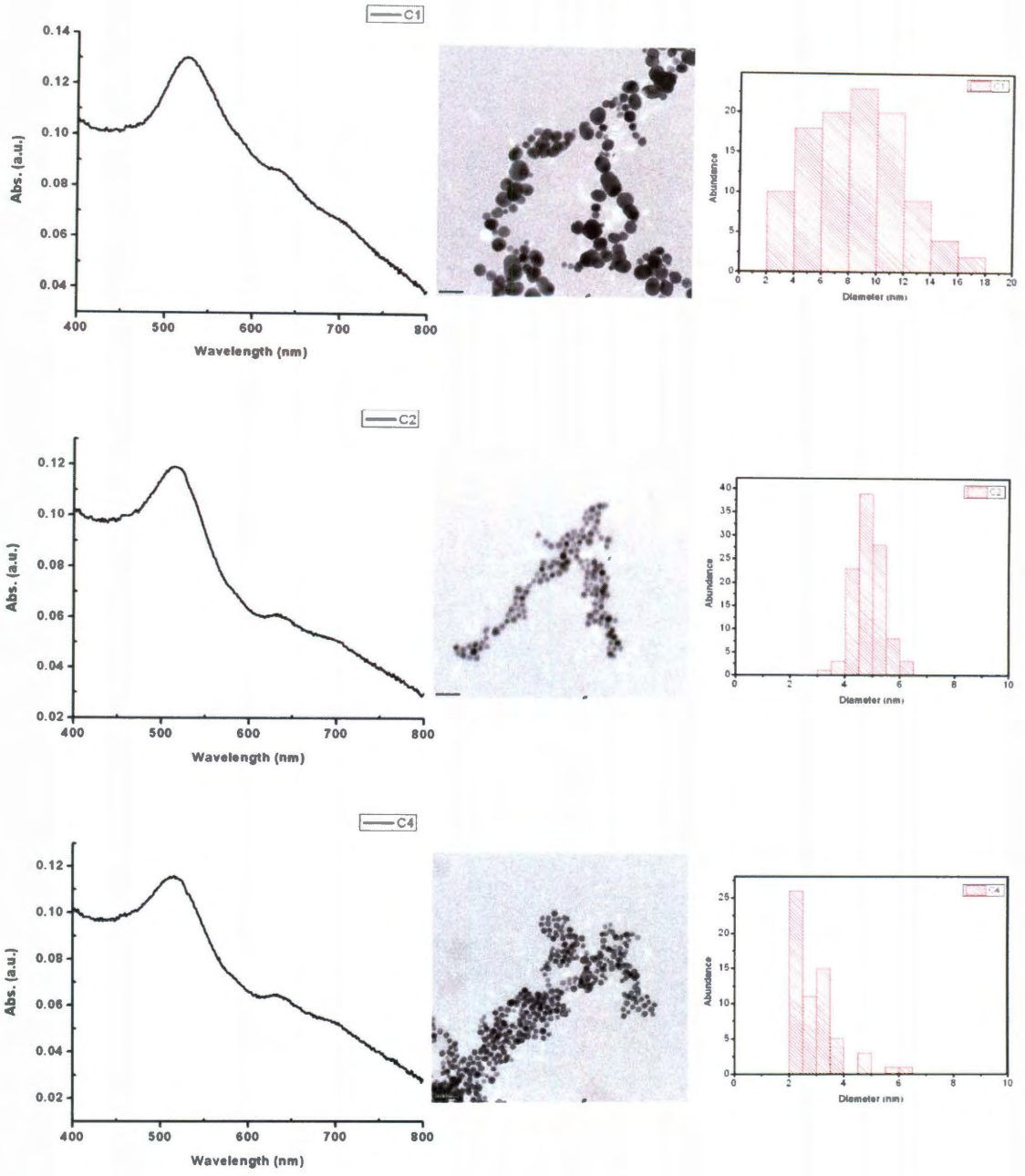

Figure 4.4. UV-visible spectra of nanoparticles synthesized from a chloroauric acid concentration of 0.3mM at flow rates of 16.9, 25.5, and 37.0 mL/min corresponding to samples C1, C2, and C4 respectively with accompanying TEM micrographs and histograms.

4.4 Formation of colloidal gold

A better understanding of the effect of the gas flow rates and chloroauric acid concentrations on nanoparticle synthesis can be had by examining the mechanisms involved in nanoparticle formation. Turkevich and others concluded that the process of particle formation was chemical in nature and involved interplay of three steps: nucleation, growth, and coagulation. They further concluded that monodispersity of the particles in a standard sol was due to a favorable juxtaposition of these three steps. Nucleation took place then stopped, then growth took over and at the same time the particles attained a stability that prevented the widening of the distribution curve by coagulation [3]. In order to understand the carbon monoxide preparation process these three steps are studied individually.

The first step to be studied, during carbon monoxide reduction of chloroauric acid, was that of nucleation. Since a particle size distribution curve is the result of a nucleation process followed by a growth process the rate curve for nucleation could be mathematically deduced from a particle size distribution curve. The rate curve, so obtained by Turkevich, had an unusual form – an induction period, an autocatalytic rise in the number of nuclei, a slowing down of nuclei formation and finally, a cessation of the nucleation process [3]. They found that gold nuclei do not form by reduction of individual gold ions to atoms which then colloid to form, by fluctuations, a stable nucleus. Rather the nucleation process consists of a polymerization step. In acid and neutral solution it is formation of gold organic polymer, in alkaline solution a polymerization of gold hydroxide may take place [3, 22]. The unimolecular redox decomposition of the organic gold polymer or the reduction of the gold hydroxide

polymer takes place when the degree of polymerization is sufficiently great to produce a stable gold particle, a particle whose cohesive lattice energy is greater than the disruptive surface energy. Once a sufficient number of nuclei are formed, the growth process takes over. This is a consequence of the following: the growth process is a one-step autocatalytic process catalyzed by the nucleus while the nucleus formation is a mutil-step process dependent on polymerization.

4.5 Preparation of monodispersed particles

The principles by which nanoparticles can be prepared are readily presented in a diagram due to LaMer Figure 4.5 [34].

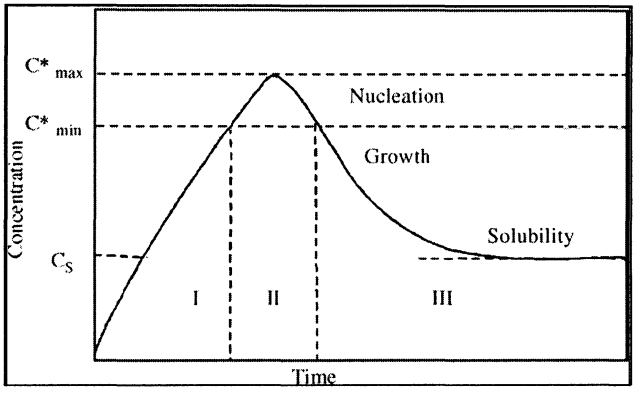

Figure 4.5. LaMer diagram.

This diagram illustrates the variation of the concentration with time during a precipitation reaction and is based on the principle that the nucleation is the limiting step in the precipitation reaction. In the first step, the concentration increases continuously with increasing time. As the concentration reaches the critical supersaturation value, between Cmax and Cmin, nucleation occurs. This leads to a decrease of the concentration. Later, the decrease of the concentration is due to the growth of the particles by diffusion. This growth occurs until the concentration reaches the solubility value. The requirements for

monodispersity are evident from the LaMer diagram. The rate of nucleation must be high enough so that the concentration does not continue to climb instead a burst of nuclei are created in a short period. The rate of growth of these nuclei must be fast enough to reduce the concentration below the nucleation concentration quickly. In this way only a limited number of particles are created. The rate of growth must be slow enough, however, that the growth period is long compared with the nucleation period. This usually narrows the size distribution, which has been the result of the finite nucleation period.

The coagulation of particles is also an important step in colloid synthesis. Its control during the synthesis process determines the shape, structure and the size distribution of the particles. Once the synthesis is complete, its absence ensures the stability of the sol. During carbon monoxide reduction of chloroauric acid two growth mechanisms could take place or a combination of the two. One mechanism suggests that nuclei are formed and that particle formation results from coalescence of the nuclei only. The second mechanism results in nuclei coalescence into simple and multiple twins and that continued monomer attachment of Au atoms further the growth of the particles. The environment in which they are exposed dictates these two dependents.

Since particle morphology is found to depend strongly on injection rates and $HAuCl_4$ concentrations a relation between $HAuCl_4$ concentration and gas-injection flow rates on particle monodispersity can be found. The effect of solution stirring speed on nanoparticle synthesis was examined and was found to play a role in nanoparticle size disparities. However, adjusting the gas injection flow rate compensated for a reduction or increase in stirring speed. Therefore the solution stirring speed is maintained at 500rpm to isolate the gas injection flow rate effect on nanoparticle synthesis. Nucleus formation and

subsequent particle growth rates are shown to depend on gas-injection flow rates as a function of HAuCl4 concentration. This phenomenon is relatively independent of the gas injection hole size as long as the liquid velocity is keep above a certain threshold.

Particle formation occurs in one of four different modes, depending on the solution $HAuCl_4$ concentration and gas flow rate. Nucleation saturation is reached during the induction phase and uniform-sized spherical particles grow in mode I for a particular $HAuCl_4$ acid concentration and matching gas flow rate. Mode II occurs when the $HAuCl_4$ concentration is sufficiently low producing non-spherical gold particulate matter regardless of gas injection velocities. Mode III occurs for high gas injection flow rates where the nucleation induction period does not reach equilibrium before particle coalescence occurs resulting in polydispersed colloidal solutions. Mode IV occurs when $HAuCl_4$ concentrations are high and gas injection flow rates are low resulting in polydispersity due to extended time in the nucleation saturation zone.

A chloroauric concentration of 0.03mM and an inlet gas flow rate of 16.9 mL/min stirred at 500 rpm resulted in coalescence and growth of nanoparticles before nucleation reached an equilibrium. In essence the induction period was initiated with a slow autocatalytic rise in the number of nuclei due to the lack of sufficient reducing agent in the solution. Because of this slow nucleus formation new nuclei were being formed while existing nuclei had already undergone coalescence resulting in polydispersity. Increasing the flow rate to 25.5 mL/min increased the autocatalytic rise in the number of nuclei. Particle growth took place after cessation of the nucleation process resulting in monodispersity. This is illustrated by the fact that the particle distribution curve for sample C2 consisted of particle sizes in the range of 4 to 6nm as opposed to the range of

2 to 17nm produced by sample C1. By increasing the flow rate further (C4) rapid coalescence of the nuclei takes place along with monomer attachment of free Au atoms to the coalesced particles. The resulting polydispersity of the sol at increased gas injection flow rates is still marginal compared to sample C1 at the reduced flow rate.

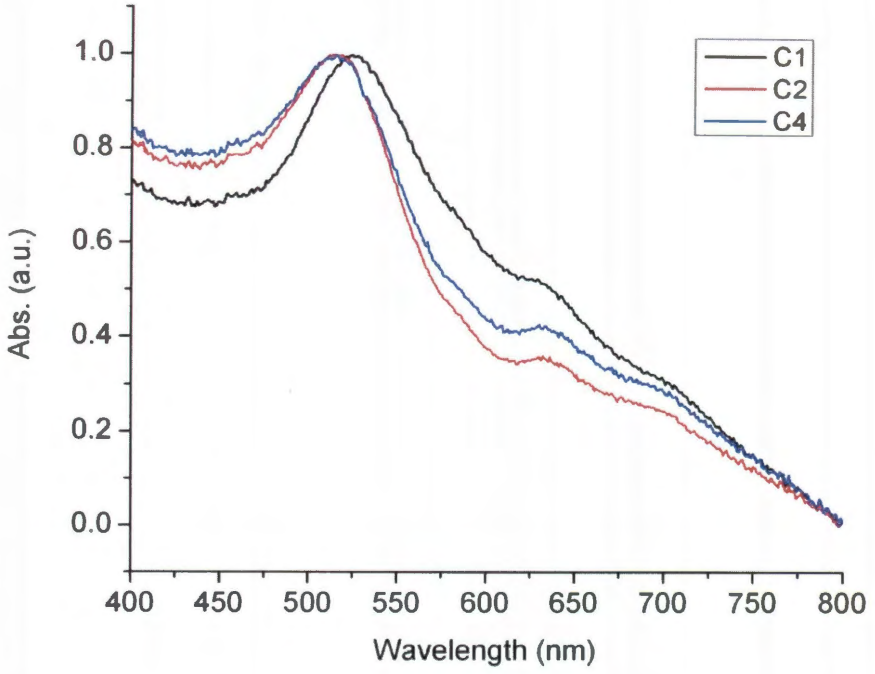

Figure 4.6. Normalized UV-visible spectra of samples C1, C2, and C4 corresponding to a sample concentration of 0.03mM and injection flow rates of 16.9, 25.5 and 37.0 mL/min respectively.

When comparing the spectra of samples C1, C2, and C4, as shown in Figure 4.6, we see that the more polydispersed sample possesses a broadened spectrum. Since the plasmon derived optical resonance of gold nanoparticles is strongly related to the dimensions of the nanoparticles and morphology a profound understanding of the mechanisms involved in surface plasmon generation is essential.

Chapter 5: Optical Response of Au Nanoparticles

5.1 Mie theory

The total extinction cross section composed of absorption and scattering is given as a summation over all electric and magnetic multipole oscillations. For nanoparticles small compared to the wavelength of the exciting light ($\lambda \gg 2r$, for gold $2r < 25\ nm$) only the dipole absorption of the Mie equation contributes to the extinction cross section σ_{ext} of the nanoparticles [10]. The Mie theory then reduces to the following relationship (quasi-static or dipole approximation) [10]:

$$\sigma_{ext} = \frac{9V{\epsilon_m}^{3/2}}{c} * \frac{\omega\epsilon_2(\omega)}{[\epsilon_1(\omega) + 2\epsilon_m]^2 + \epsilon_2(\omega)^2}\ , \tag{25}$$

where V is the spherical particle volume, c the speed of light, ω the angular frequency of the existing radiation, and ϵ_m is the dielectric constant of the surrounding medium (assumed to be frequency independent). $\epsilon_1(\omega)$ and $\epsilon_2(\omega)$ denote the real and imaginary part of the dielectric function of the particle material, respectively

$$\epsilon(\omega) = \epsilon_1(\omega) + i\epsilon_2(\omega)\ . \tag{26}$$

From eq 25 it follows that resonance occurs when $\epsilon_1(\omega) \approx -2\epsilon_m$ if ϵ_2 is small or only weakly dependent on ω. The bandwidth and peak height are roughly determined by $\epsilon_2(\omega)$[5]. Within the Drude-Lorentz-Sommerfeld free-electron model $\epsilon(\omega)$ is given by

$$\epsilon(\omega) = 1 - \frac{{\omega^2}_p}{\omega^2 + i\gamma\omega}\ , \tag{27}$$

where the plasma frequency $\omega_p = (ne^2/\varepsilon_0 m_{eff})$ depends on the electron density n and on the proper electron effective mass m_{eff}.

However, within the dipole approximation there is no size dependence except for a varying intensity due to the fact that the volume V depends on the particle radius R. Experimentally; one however observes a strong size dependence of the plasmon bandwidth [5].

5.2 Intrinsic size effects

As a modification to the Mie theory for small particles, the dielectric function of the metal nanoparticles itself is assumed to become size dependent $[\epsilon = \epsilon(\omega, r)]$ and therefore rendering a size-dependent absorption cross section even within the dipole approximation (intrinsic size effects) [10]. In the classical theory for free-electron metals with infinite boundaries, the damping is due to electron-electron, electron-phonon, and electron-defect scattering processes. γ is therefore closely related to the electrical resistivity of the metal and one can express γ as the sum over all reciprocal relaxation times [5]. For the bulk the electron-phonon term is the dominating one and γ should be a constant. However, for small particles this is not valid. The classical free path effect model argues that if the particle size becomes comparable to the mean free path of the electrons the surface becomes a scatterer due to interactions of the conduction electrons with the particle surface. This additional collision process results in a reduced effective mean free path and increased γ which now depends on particle size

$$\gamma(r) = \gamma_0 + \frac{Av_F}{r}, \tag{28}$$

where $\gamma_0$is the bulk damping constant and A includes details of the scattering processes [10].

This classical picture of the limitation of the MFP due to surface scattering has been suggested by Kreibig and results in a 1/r dependence of the plasmon bandwidth.

A 1/r dependence of the plasmon bandwidth is furthermore predicted by a more recent quantum mechanical theory by Persson [35] considering the chemical nature of the nanoparticle surrounding interface. Following this model, an additional broadening of the plasmon band is caused but the transfer of the excitation energy into adsorbate levels located above the Fermi level. This model is therefore called chemical interface damping. Chemical interface effects could thus be isolated from size effects. The corrected dielectric function for the particle material is given by the inclusion of the size dependent term:

$$\epsilon(\omega, r) = \varepsilon_{bulk}(\omega) + \frac{{\omega^2}_p}{\omega^2 + i\gamma_0\omega} - \frac{{\omega^2}_p}{\omega^2 + i\omega(\gamma_0 + \frac{Av_F}{r})} \quad . \tag{29}$$

The optical response of the AuNPs, shown in Figure 4.6, illustrates the size dependent broadening effects. A contribution to the plasmon bandwidth can also be attributed to inhomogeneous broadening as a result of the AuNP size distribution as evident in the TEM images of Figure 4.4. The larger the standard deviation for a AuNP solution the more inhomogeneous broadening contributes to the overall plasmon bandwidth.

5.3 Extrinsic size effects

For larger nanoparticles (2r > 25nm) the extinction cross section is also dependent on higher-order multipole modes within the full MIE equation and the extinction spectrum is then also dominated by quadrupole and octopole absorption as well as scattering [5-6, 8, 10]. These higher oscillation modes explicitly depend on the particle size and with increasing size the plasmon absorption maximum is shifted to longer wavelength and the

bandwidth increases. The total plasmon band absorption is then the superposition of all contributing multipole oscillations peaking at different energies. The excitation of the higher-order modes is explained in terms of an inhomogeneous polarization of the nanoparticles by the electromagnetic field as the particle size becomes comparable to the wavelength of the exciting radiation. The broadening of the plasmon band is then usually ascribed to retardation effects [5, 10]. On the other hand, the increased line width or equivalently the faster loss of coherence of the plasmon resonance could qualitatively also be described as a result of the interactions between the dipole and the quadrupole oscillatory motions of the electrons, thus destroying the phase coherence. As the size effect enters through the full MIE equation and the complex dielectric function of the bulk material, which is no longer size dependent, is used, this behavior of the plasmon resonance is regarded as an extrinsic size effect [10].

The nanoparticles synthesized in samples C1-C5 are less than 25nm so they are described by intrinsic size effects. The broad spectrum of sample C1 can be described as a summation of electromagnetic resonances due to inhomogeneous size distribution of the nanoparticles. When the chloroauric acid concentration was further increased to 0.1mM in 0.01mM increments a gradual increase in nanoparticle size from 4.6 to 6.7nm was observed.

Chapter 6: Synthesis Variables

6.1 Nanoparticles prepared at different gas injection flow rates

When the chloroauric concentration approached 0.2mM the gas injection flow rate had a less pronounced effect on the spectra symmetry, however, the flow rate continued to dictate the monodispersity of the particles. Figure 6.1 shows the UV-visible spectra of gold nanoparticles synthesized from a chloroauric acid concentration of 0.3mM (sample set M). The most monodispersed sample for set M was produced at a gas injection flow rate of 25.5 mL/min (M2). The mean particle diameter for M2 was 9nm with a standard deviation of 11%.

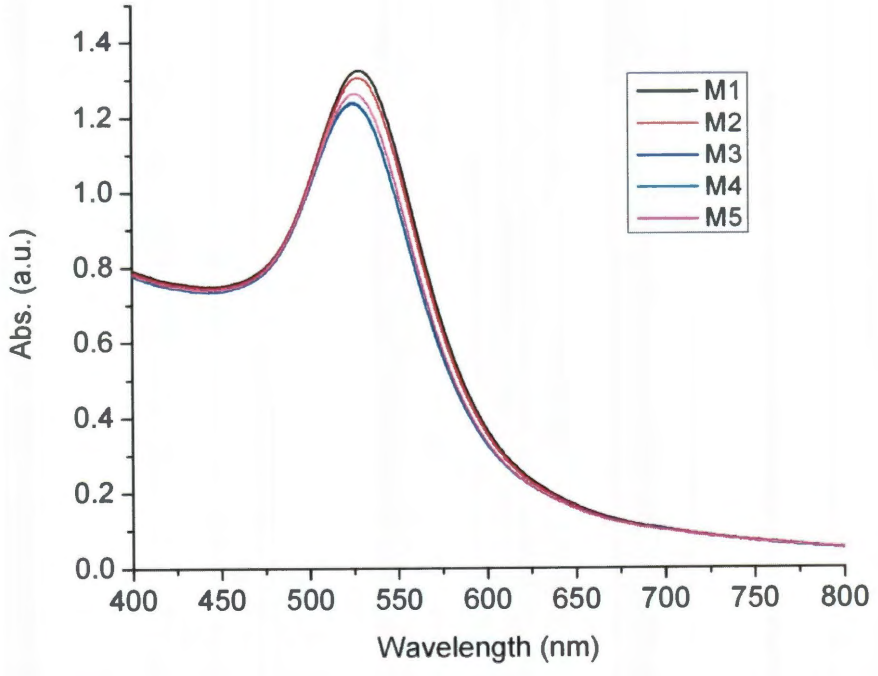

Figure 6.1. UV-visible spectra of gold nanoparticles synthesized from a chloroauric acid concentration of 0.3mM.

The most monodispersed particles were produced with gas injection flow rates between 25.5 and 37 mL/min. For the following discussion spectra from samples resulting in monodispersed particles with the lowest standard deviation are obtained from each concentration set.

6.2 Increasing $HAuCl_4$ concentration

As the concentration increased to 0.5mM, 20 to 25nm particles were produced. Continual increase of the chloroauric acid concentration beyond 0.5mM to 0.6mM only produced small changes in nanoparticle size with increased absorbance. The standard deviation for the sol at 0.6mM was 8% indicating monodispersity. As the concentration was increased to 1mM nanoparticles approaching 30 nanometers were produced however the mean standard deviation approached 20%. Further doubling the concentration to 2mM had no uniform effect on particle growth with the majority of the particles in the 30nm size regime however some 40 to 55nm particles were produced with a standard deviation approaching 35%. If we examine the UV-visible spectra of the sol prepared at different concentrations Figure 6.2, increasing from 0.02mM to 1mM, we see an increase in absorbance that correlates to an increase in particle concentration and volume. Figure 6.3 shows the pronounced red shifting of the plasmon that is associated with increased nanoparticle size that is in line with the prediction described by MIE theory.

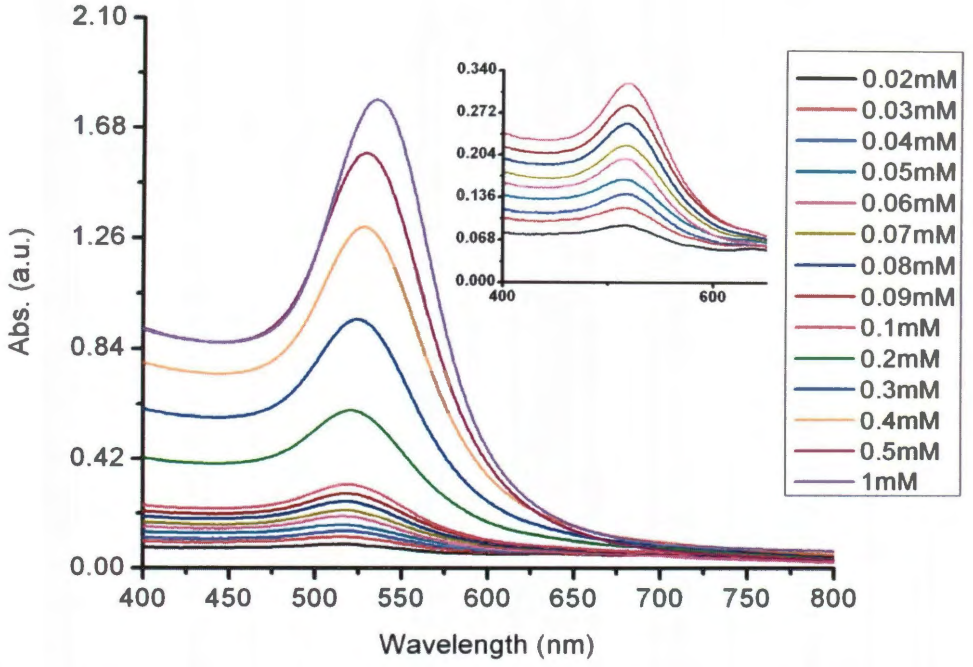

Figure 6.2. UV-visible spectra of gold nanoparticles with increasing chloroauric acid concentrations from 0.02mM to 1mM. The inset the absorbance spectra of gold nanoparticles produced from concentrations of 0.02mM to 0.1mM.

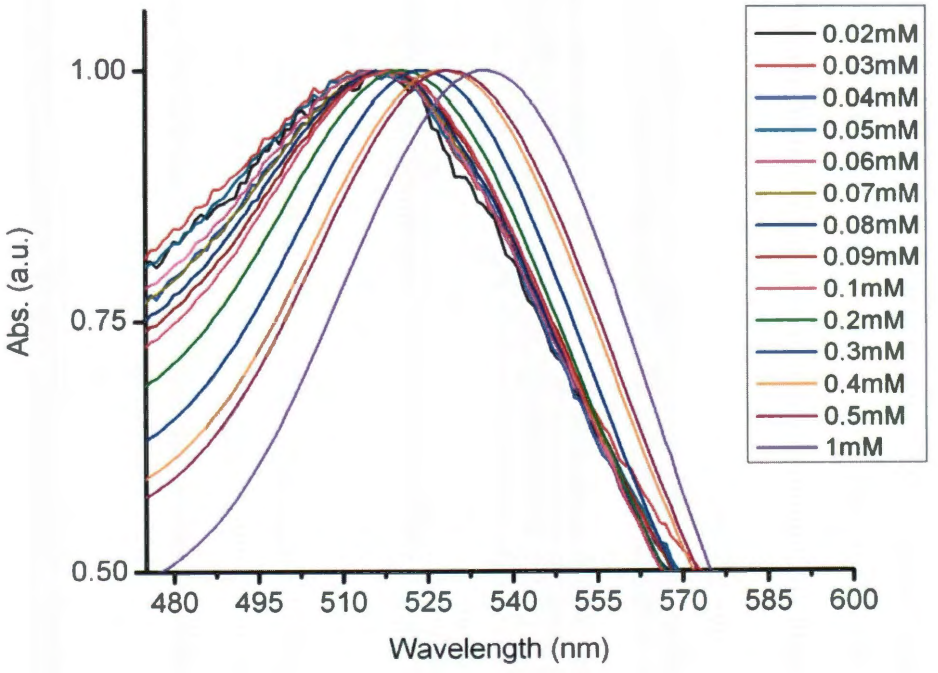

Figure 6.3. Normalized UV-visible spectra of gold nanoparticles with increasing chloroauric acid concentrations from 0.02mM to 1mM. A red-shifting of the plasmon is observed as the chloroauric acid concentration is increased.

Figure 6.4 shows the plasmon peak position and absorbance plotted against chloroauric acid concentration. As the chloroauric acid concentration increases the particle plasmon shifts towards the red along with an increased absorbance due to larger particle size and increased particle concentration.

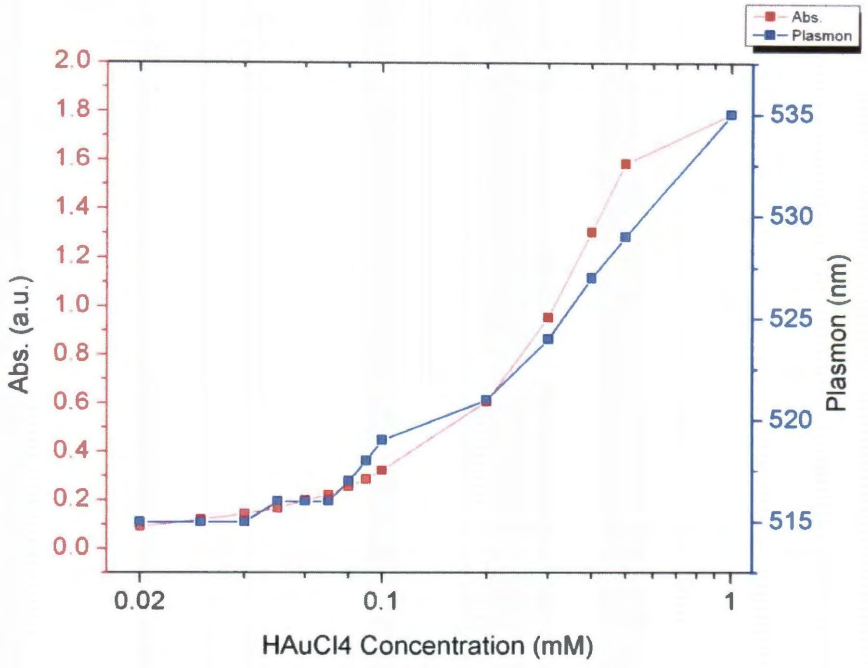

Figure 6.4. Plasmon peak position and absorbance value at chloroauric acid concentrations ranging from 0.01mM to 1mM. The data is plotted on a logarithmic scale.

Table 6.1 summarizes the data of the most monodispersed samples for concentrations 0.02 to 1mM $HAuCl_4$. The particle diameter and the mean standard deviation as well as the SPR peak position and its maximum are given. The statistical analysis of the particles for samples ranging from 0.02 to 0.6mM $HAuCl_4$ concentrations reveals an average size distribution of about 11%.

Table 6.1: Summary of the size and size distribution of the Au nanoparticles

HAuCl4 concen. [mM]	Diameter [nm]	Mean Standard Deviation [%]	λ_{max} [nm]	HAuCl4 concen. [mM]	Diameter [nm]	Mean Standard Deviation [%]	λ_{max} [nm]
0.02	5.2	11	515	0.1	6.7	15	519
0.03	4.6	7	515	0.2	6.4	13	521
0.04	4.7	12	515	0.3	8.5	10	524
0.05	5.4	16	516	0.4	9	11	527
0.06	5.7	13	516	0.5	15	10	529
0.07	5.3	11	516	0.6	25	8	530
0.08	5.4	11	516	1	45	18	535
0.09	6.6	15	518	1	55	22	543

Chapter 7: Influence of Speciation of $HAuCl_4$ on the Synthesis of AuNPs

7.1 Influence of pH on Au nanoparticle synthesis

Since the synthesis process takes place in an acid environment the particle is formed of gold organic polymer with a small contribution from gold hydroxide polymer reduction. As the concentration of chloroauric acid increases the pH of the solution decreases. Figure 7.1 shows the solution pH before and after synthesis as a function of chloroauric acid concentration.

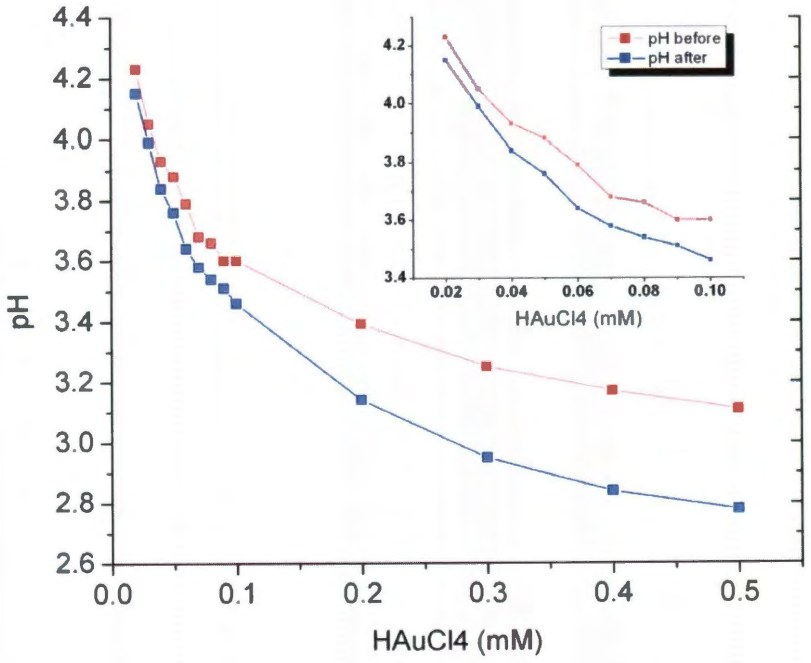

Figure 7.1. pH value per chloroauric acid solution concentration ranging from 0.02mM to 0.5mM. The inset shows pH values for concentrations 0.02mM to 0.1mM. All pH measurements were taken at 22C.

An effective monodispersed particle size threshold, in which the standard deviation remained below 13%, was reached at approximately 25nm. As previously mentioned, continual increase of the chloroauric concentration eventually resulted in adverse affects on nanoparticle monodispersity.

The pH of aqueous $HAuCl_4$ usually varies in different approaches for the synthesis of Au colloids. It is known that pH is a factor influencing the nucleation and growth of Au colloids [8, 22]. To further grow particles and maintain monodispersity $HAuCl_4$ hydrolysis is explored. We systematically investigated the addition of potassium carbonate (K_2CO_3) to generate an alkaline solution for gold hydroxide polymer reduction via carbon monoxide and found that the speciation has great influence on the size and thus properties of Au colloids. As the pH increases speciation of aqueous $HAuCl_4$ takes place that varies with varying pH.

Adding potassium carbonate raises the pH of the solution allowing hydrolysis of $HAuCl_4$ to take place to form gold hydroxide solution. A 200mL aqueous $HAuCl_4$ solution, with a concentration of 0.1 mM, was prepared by adding fresh gold to 200mL of DI water. The pH was measured to be 3.6. This solution was aged in an amber bottle in a light protected 4°C environment for a minimum of 72 hours prior to use. A 0.5N stock solution of potassium carbonate was prepared and stirred for a minimum of one hour. After aging, the chloroauric acid solution was allowed to gradually rise to 22°C. $HAuCl_4$ aqueous solutions with various pH values were prepared by the addition of certain amounts of K_2CO_3 aqueous solution into 20mL of $HAuCl_4$ aqueous solution and shaken vigorously for a minimum of one minute. This solution was allowed to age for a 15

minutes before introduction of carbon monoxide gas. The pH values of the aqueous solutions, measured prior to reduction, ranged from 4.25 to 11.4.

Figure 7.2 shows UV-visible absorption spectra of Au colloid solutions prepared by reduction of aqueous $HAuCl_4$ by carbon monoxide at various pH. At pH = 4.25, the acquired Au colloids exhibit a symmetric SPR peak at 512nm. With pH increasing to 6.6 there is a SPR shift to 527nm. With the pH increasing to 7.45, the SPR peak position for acquired Au colloids does not change much at 528nm as shown in Figure 7.3. The SPR peak remains symmetric. The SPR feature of Au colloids changes abruptly when the pH of aqueous $HAuCl_4$ is 9.34 showing a broad feature originating at 559nm. The SPR peak further red shifts when the pH value increased to 10.3 and absorption in the NIR region also gained significant intensity.

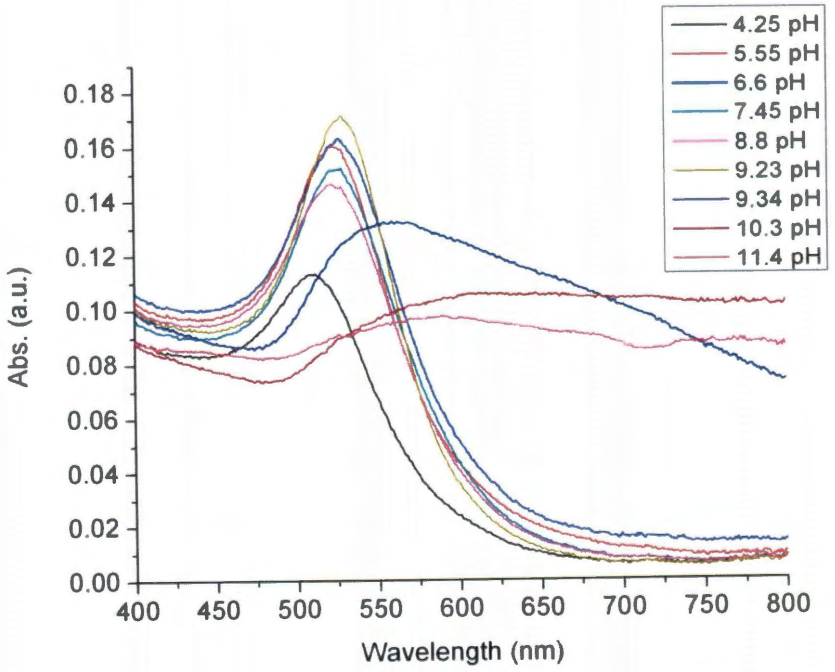

Figure 7.2. UV-visible spectra of Au colloid solution synthesized at varying pH values.

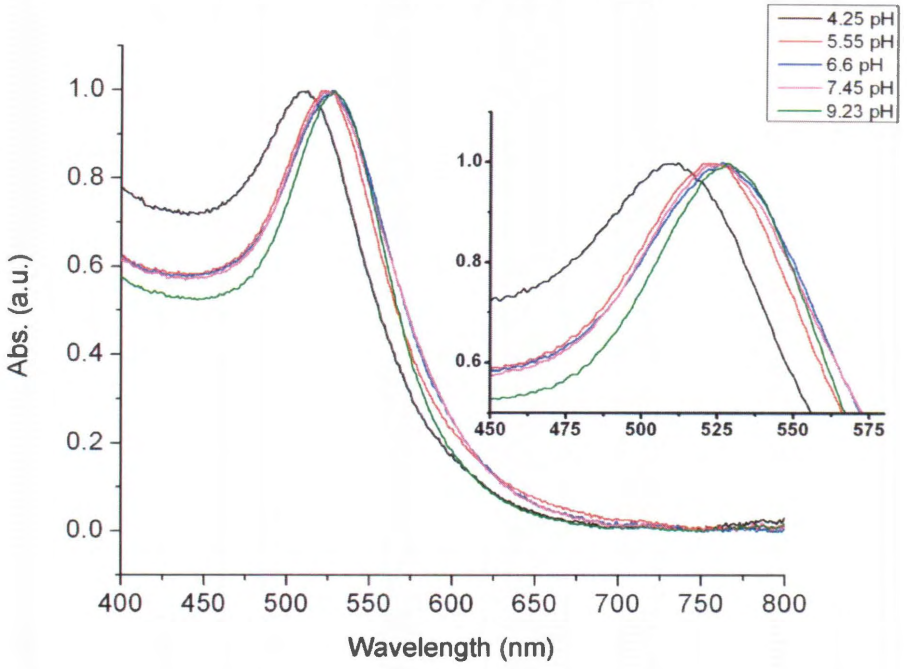

Figure 7.3. Normalized UV-visible spectra of Au colloid synthesized at a pH of 4.25, 5.55,6.6, 7.45, and 9.23. The inset illustrates the small SPR peak change from 5.55 to 7.45.

Table 7.1 shows the influence of pH upon stability of the particles at various times up to 2 months.

TABLE 7.1: Influence of pH upon stability of Au colloids

pH Before Synthesis	pH After Synthesis	Color	Stability (After 1 Hour at room temperature)	Stability (After 6 Hours at room temperature)	Stability (After 2 Months at 4°C)
4.25	3.72	Light pink	Stable	Stable	Small aggregation
5.55	4.75	Light red	Stable	Stable	Small aggregation
6.6	5.92	Light Red	Stable	Stable	Stable
7.45	6.11	Light Red	Stable	Stable	Stable
8.8	6.42	Light Red	Stable	Stable	Stable
9.23	6.55	Medium Red	Stable	Stable	Stable
9.34	6.32	Purple	Stable	Stable	Medium aggregation
10.3	8.10	Blue	Stable	Some Aggregation	Heavy aggregation
11.4	10.96	Light Blue	Crashed	Crashed	Crashed

7.2 Speciation of Aqueous $HAuCl_4$

Previous experimental and theoretical results demonstrate that $AuCl_4^-$ undergoes a pH-dependent stepwise hydrolysis [20, 22, 28] which gives way to $[AuCl_x(OH)_{4-x}]^-$. The extent of hydrolysis in turn depends on the pH that gives an indication of the amount of OH^- available for hydrolysis. When the pH is low, approximately 3, $[AuCl_4]^-$ ions dominate the solution. As the pH is increased to 4.25 $[AuCl_4]^-$ concentration is lowered and a noticeable contribution from $[AuCl_3(OH)]^-$ ions is observed. Raising the pH of the solution to 6.66 reduces the concentration of $[AuCl_4]^-$ and $[AuCl_3(OH)]^-$ significantly and is primarily made up of $[AuCl_2(OH)_2]^-$ ions. Further increasing the pH to 8.8 results in

large ion contribution from $[AuCl(OH)_3]^-$ ions. Further raising the pH to 10.3 results in an overwhelming ion contribution from $[Au(OH)_4]^-$ ions with an appreciable contribution from $[AuCl(OH)_3]^-$ ions. This is due to the fact that $Au(OH)_3$ is amphoteric, its solubility increases due to the formation of $[Au(OH)_4]^-$ at higher pH, thus making the soluble $[Au(OH)_4]^-$ the most dominant species at high pH [29] instead of the precipitating $[AuCl(OH)_3]^-$. It is the control of hydrolysis to tune the speciation of $[AuCl_x(OH)_{4-x}]^-$ that subsequently influence the nanoparticle size.

Amongst the six species of $[AuCl_x(OH)_{4-x}]^-$ discussed earlier, $[Au(OH)_4]^-$ seems to have the lower tendency to be reduced in solution to form colloidal gold which is evident from its slow and gradual color change when reduced. This is in contrast to the reduction of other $[AuCl_x(OH)_{4-x}]^-$ species formed at lower pH where we observed that the addition of carbon monoxide causes a color change within 2 minutes to form colloidal gold. This observation may possibly be attributed to a weaker reduction potential of $[Au(OH)_4]^-$ compared to other species. We found that adjustment to other pH < 10 by addition of smaller amounts of K_2CO_3 results in the formation of other dominant species that have greater tendency to be reduced in solution to form colloidal gold.

It was observed that hydrolysis of $[AuCl_4]^-$ occurred within minutes after the addition of K_2CO_3 indicating immediate formation of the $[AuCl_x(OH)_{4-x}]$ species. It was further observed that Au colloid, of varying sizes, was produced when K_2CO_3 and $HAuCl_4$ concentrations and gas injection flow rates remained constant and only aging times varied. This indicated that aging the gold hydroxide solution, before the addition of carbon monoxide gas, had a strong influence on the outcome of the reaction.

The effect of aging on $[AuCl_4]^-$ hydrolysis was further explored by adding 25mg of K_2CO_3 to a 200mL 0.38mM $HAuCl_4$ aqueous solution. Figure 7.4 shows the UV-visible spectrum of Au colloid synthesized from this solution. Samples were taken and reduced with carbon monoxide gas at various time points.

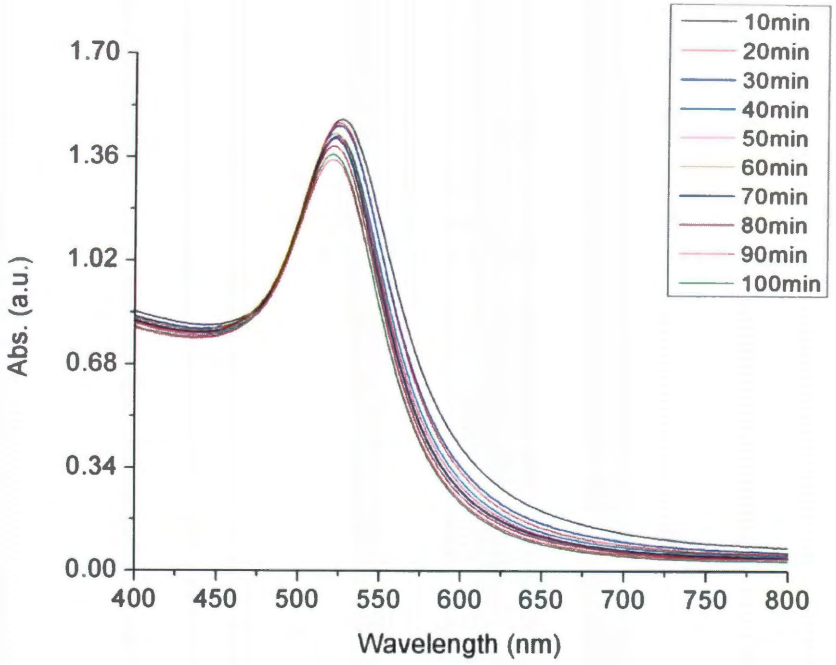

Figure 7.4. UV-visible spectra of Au colloid produced from aqueous $K_2CO_3/HAuCl_4$ solution aged in increments of 10 minutes.

Figure7.5 shows the SPR shift of the Au colloids synthesized at various time points. We observe that the plasmon blue shifts from 527nm to 521nm within the 80 minutes. The SPR peak position then remains constant however the SPR peak width narrows and diminishes as time progresses. We observed that even after 23 hours the SPR peak position remained at 521nm. However, at an aging time of 48 hours the SPR red shift to 522nm and at 120 hours the aging effect reached a steady state of 524nm. Even at an aging period of 138 hours the aqueous solution still produced and SPR peak at 524nm.

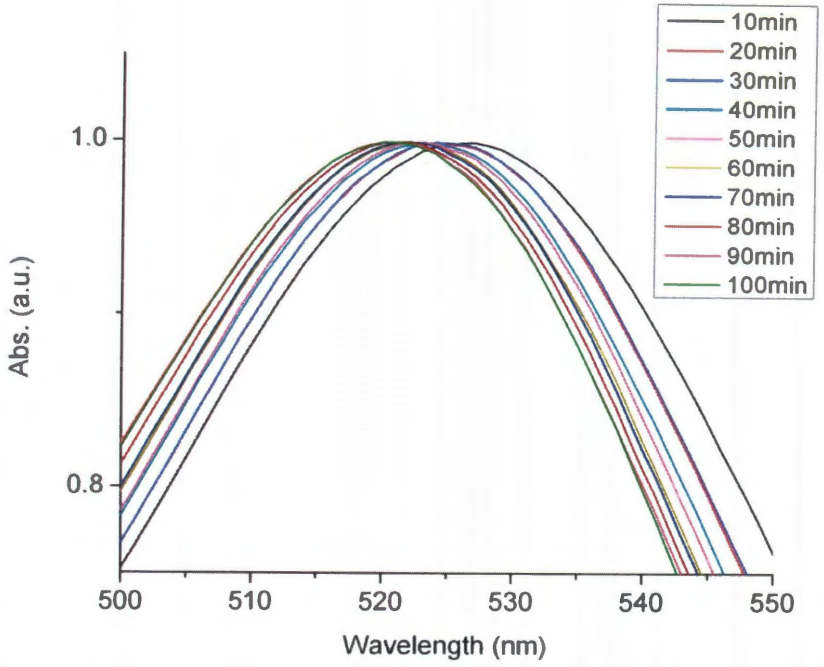

Figure 7.5. Normalized UV-visible spectra of Au colloid produced from aqueous K_2CO_3/$HAuCl_4$ solution aged in increments of 10 minutes.

These results illustrate that a minimum time is required for complete hydrolysis of $[AuCl_4]^-$ to take place and an equilibrium between $[AuCl_x(OH)_{4-x}]$ species to form. The effective time required is found to be dependent on chloroauric acid concentration and pH of the aqueous solution. By controlling the development of the $[AuCl_x(OH)_{4-x}]$ species colloids of various sizes can be synthesized using carbon monoxide as a reducing agent. When the pH is sufficiently high the resultant aging process can generate coalescence of $Au(OH)_3$ particles initiating a nucleation process absent of a reducing agent. This nucleation process is out of favor with the requirements necessary for generating monodispersed Au colloid. Thus proper aging times must be determined to synthesize monodispersed nanoparticles of a particular size from a given K_2CO_3 and $HAuCl_4$ concentration. Exploiting the control of $[AuCl_x(OH)_{4-x}]$ species development, by

addition of K_2CO_3 and aging of the solution, Au colloid in the ranges of 15 to 80nm in diameter were produced.

Figure 7.6 shows UV-visible spectra of Au colloid produced from a mixture of 200mL 0.38mM $HAuCl_4$ aqueous solution and 75mg of K_2CO_3 aged at 30 and 40 minutes. Both SPR peaks were well ordered with a SPR peak position of 536nm for the 30 minute aged solution and 546nm for the 40 minute aged solution. Both solutions were aerated with CO gas at an inlet gas flow rate of 25.5 mL/min. The red-shift and dampening of the SPR peak indicates an increase in particle size.

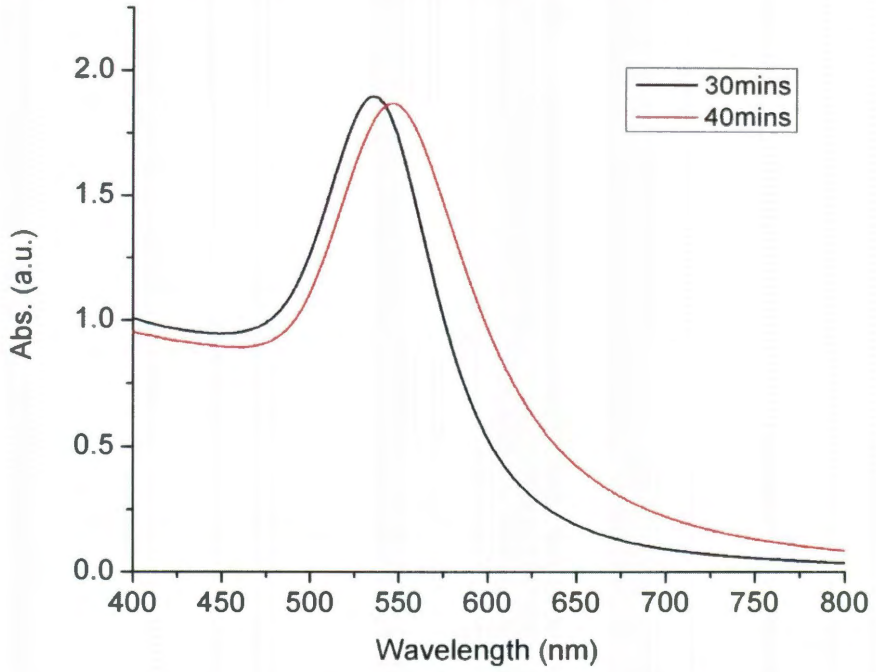

Figure 7.6. UV-visible spectra of Au colloid produced from a mixture of 0.38mM HAuCl4 aqueous solution and 75mg of K_2CO_3 aged at 30 and 40 minutes.

We observed that it was possible to increase the amount of K_2CO_3 in a $HAuCl_4$ aqueous solution of known concentration while decreasing the aging time produced monodispersed Au colloid. Figure 7.7 shows UV-visible spectra of Au colloid produced from a 200mL 0.38mM $HAuCl_4$ aqueous solution with 100mg of K_2CO_3 aged for 30

minutes. The amount of solution aerated had a small but noticeable effect on SPR peak position and intensity. The resulting SPR peak positions were 550, 553, and 554nm for synthesis volumes of 20, 40, and 50mL respectively.

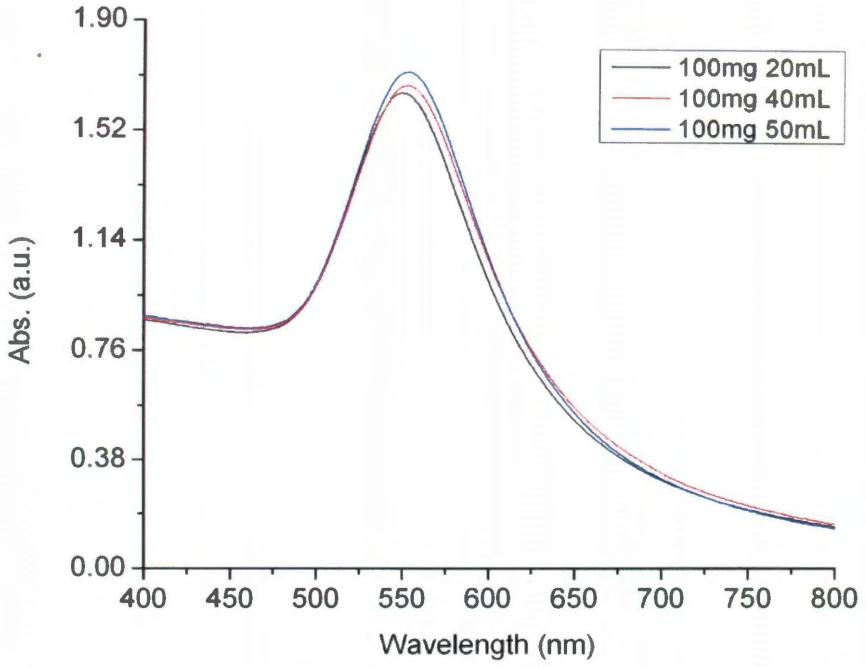

Figure 7.7. UV-visible spectra of Au colloid produced from a 200mL 0.38mM HAuCl4 aqueous solution with 100mg of K_2CO_3 aged for 30 minutes at aeration volumes of 20, 40, and 50mL.

0.38mM $HAuCl_4$ aqueous solutions with 75mg and 100mg of K_2CO_3 aged for 30 minutes produced Au colloid with SPR peak positions at 536 and 553nm respectively.

By employing a combination of gold polymer reduction and gold hydrolyzed polymer reduction, particles sizes from ~4 to 100 nm can be synthesized. Figure 7.8 shows a TEM micrograph illustrating the different sizes available using CO as a reducing agent. Figures 7.8A, B, C, D are TEM images of AuNPs synthesized without the addition of K_2CO_3. Figures 7.8E,F are AuNPs synthesized from a hydrolyzed solution of aqueous $HAuCl_4$ via the addition of K_2CO_3. The corresponding sizes of the AuNPs are 4, 6, 15, 25, 50, and ~100 nm with standard deviations of 7, 13, 8, 8, 10, and 11%, respectively.

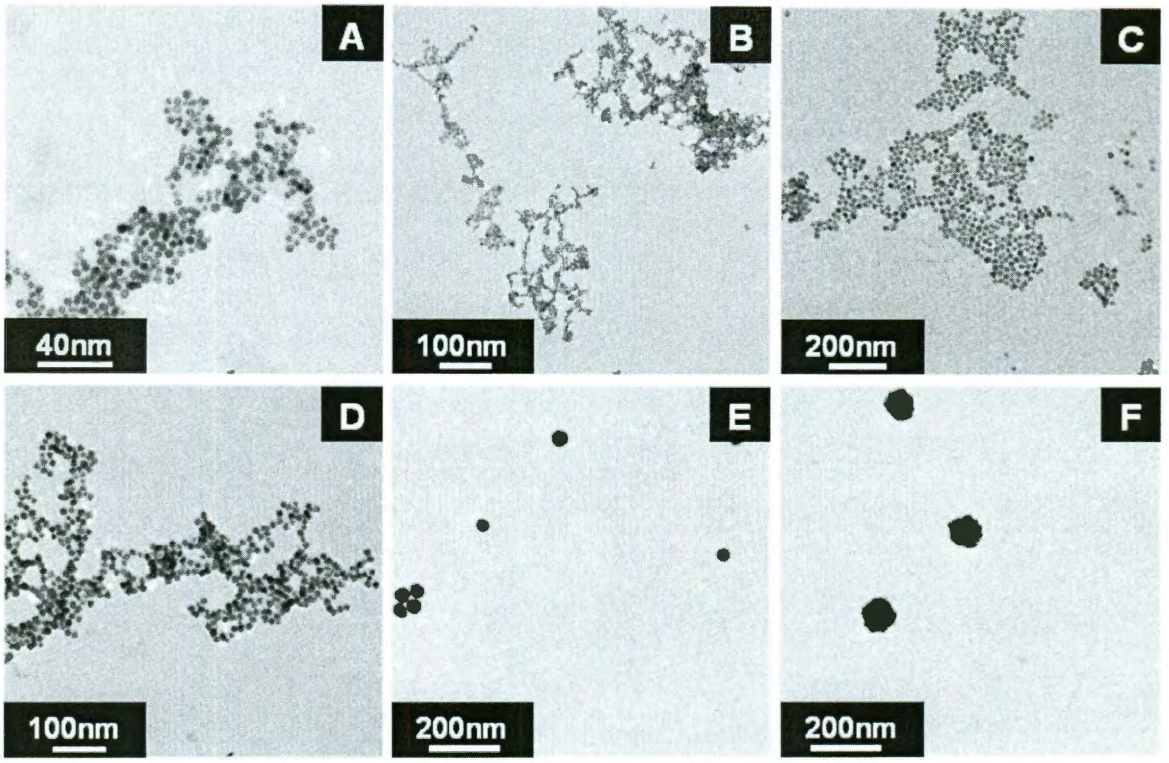

Figure 7.8 A, B, C, and D are TEM images of AuNPs synthesized without the addition of K_2CO_3. E and F are AuNPs synthesized from a hydrolyzed solution of aqueous $HAuCl_4$ via the addition of K_2CO_3. The corresponding sizes of the AuNPs are 4, 6, 15, 25, 50, and ~100 nm respectively.

Chapter 8: Alternate Synthesis Methods for Au Nanoparticles

8.1 Synthesis of Au colloid using citrate

Other Au colloid synthesis methods exist and it is possible to increase particle size as a function of $HAuCl_4$ concentration and reducing agent concentration. As previously mentioned a typical and widely used method is based on the reduction of tetrachloroaurate ions in water using sodium citrate as a reductant to obtain AuNPs with diameters ranging from 16 to 147nm [3]. This method has shown a good control over the particle size, but good monodispersity is limited to the synthesis of larger particles typically in the range of 25 to 120 nm. Gold nanoparticles of various sizes were produced via addition of sodium citrate at different concentrations. Citrate based gold nanoparticles are prepared following a modified method introduced by Turkevich. 1% trisodium citrate solution was made by dissolving 0.5g trisodium citrate in 50mL MilliQ water and vigorously vortexed for a minimum of one minute. 1.0 mM solution of hydrogen tetrachloroaurate trihydrate was made by dissolving 0.078766g of $HAuCl_4$ to 200mL of MilliQ water and vigorously vortexed for a minimum of two minutes. 20mL of 1.0mM HAuCl4 solution was added to a 50mL beaker. The solution is subsequently stirred and heated just to a boil. Once the solution is boiling 2mL of 1% solution of trisodium citrate dehydrate is added. Alternative solutions of 0.25%, 0.75%, 0.9%, and 1.05% citrate were prepared by adding 0.125g, 0.375g, 0.45g, and 0.525g to 50mL MilliQ water respectively. A UV-visible spectrum was taken for each sample Figure 8.1.

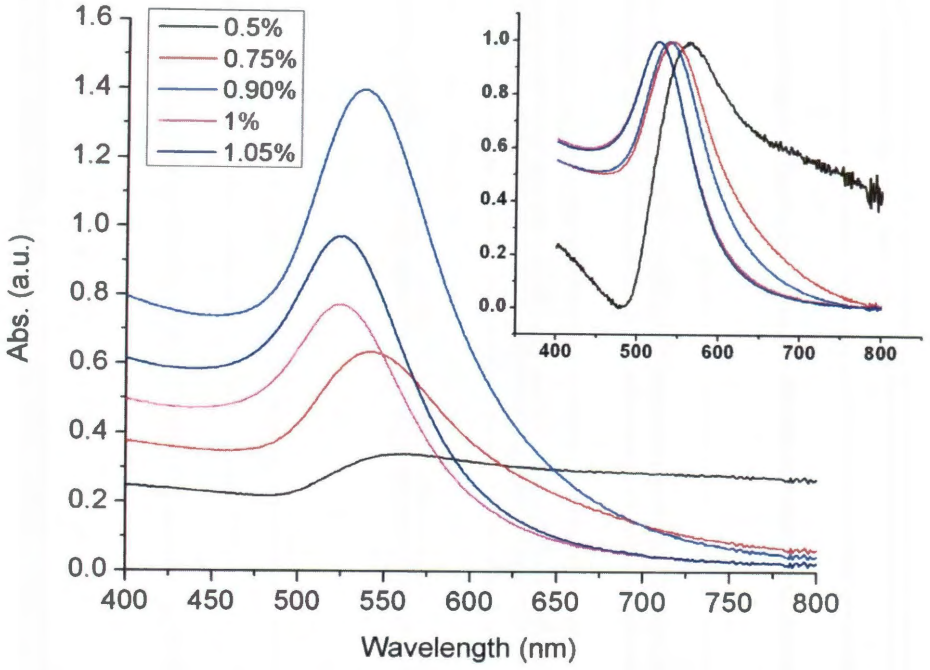

Figure 8.1. UV-visible spectra of Au colloid produced by varying the concentration of citrate.

The UV-visible spectrum indicates that varying the citrate concentration while keeping the $HAuCl_4$ concentration constant affects nanoparticle size and thus monodispersity. Adding 2mL of 0.5% solution produced a very polydispersed sample with a dampened SPR peak. This is due to the lack of adequate citrate in the solution to produce effective nuclei particle counts and reduce free $AuCl_4$- in the remainder of the solution. As the citrate concentration is increased to 0.75% more reducing agent is available however a broadened SPR peak is present. The optimum citrate % wt is found to be 0.90%. Polydispersity of the sample can be examined by examining the UV-visible spectra and determining the SPR bandwidth. Figure 8.2 shows the SPR peak position, absorbance intensity, and FWHM as a function citrate concentration.

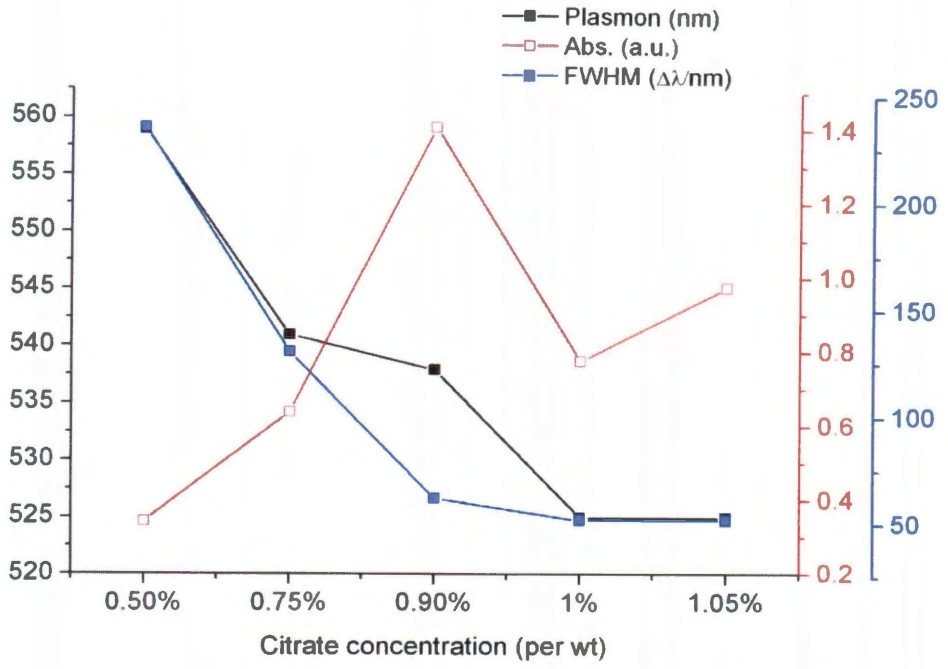

Figure 8.2. The SPR peak position, absorbance intensity, and FWHM as a function citrate concentration.

These results indicate that as the citrate concentration increases the SPR peak red-shifts and the full width half max decreases. The smaller the FWHM value the more monodispersed the Au colloid. The max absorbance value is obtained at a citrate concentration of 0.90% and the SPR peak position remains red while an increase of citrate concentration to 1% and 1.05% decreases the absorbance intensity and blue shifts the peak.

8.2 Synthesis of Au colloid using formaldehyde

Formaldehyde based gold nanoparticles are prepared by adding 3mL 1% wt $HAuCl_4$ solution to 200mL of MilliQ water and shaking vigorously for a minimum of 30 seconds. 50mg of anhydrous potassium carbonate was then added to the solution and shaken vigorously for a minimum of one minute. This process was repeated so that two 200mL

potassium carbonate gold salt stock solutions were available. The solutions were then aged and at different time points. 3mL of stock solution was aliquot into several cuvettes. Different concentrations of formaldehyde were added to each cuvette ranging from 7.5uL to 50uL. The cuvettes were subsequently capped, bundled and shaken for a period of 2 minutes. The solution was allowed to sit for another 2 minutes to ensure all possible Au_3 was reduced. Upon reduction of the Au^3 ions to Au^0 a visible color change was present. A UV-visible spectrum was taken for each sample Figure 8.3.

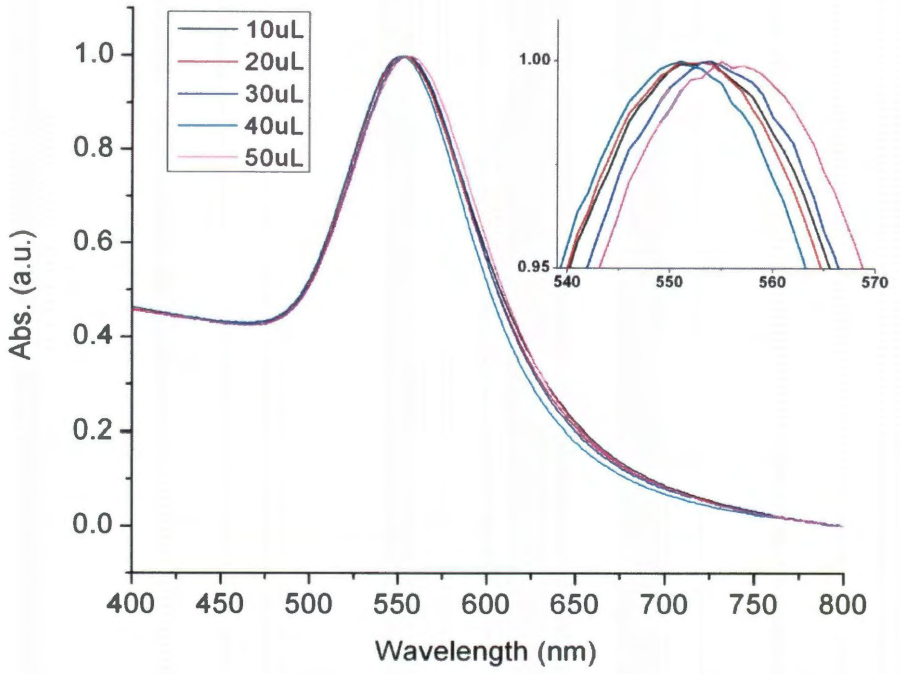

Figure 8.3. UV-visible spectra of Au colloid synthesized with varying concentrations of formaldehyde ranging from 10 to 50uL in 10uL increments. The inset is a normalized view of the SPR peak.

Synthesizing Au colloid by formaldehyde reduction produced symmetric spectra; however increasing the formaldehyde 5 fold only produced a 4nm SPR peak shift. The plasmon bandwidth also remained relatively unchanged with increased reductant. These results indicate that varying the reducing agent offers no control over Au nanoparticle

size. The excess formaldehyde left in the solution also aggregated the nanoparticles after a short time.

8.3 Nanoparticles prepared via seeded growth

Seeded growth of Au nanoparticles is another popular method to increase nanoparticle size. To obtain seed colloids, 1mL of 1% $HAuCl_4$ solution was mixed with 100mL of DI water. 1mL of 1% citrate solution and 1mL of 0.75% NaBH4 were successively added to the mixture, and the stirring times were 1 minute and 5 minutes respectively. To examine the effect of seed population on Au nanoparticle synthesis using carbon monoxide as a reducing agent varying amounts of seed particles were added to 20mL 0.38mM $HAuCl_4$ aqueous solutions. Figure 8.4 shows the UV-visible spectra of Au colloid synthesized by carbon monoxide gas with addition of seed particles. The seed concentrations varied from 200uL to 400uL. The aqueous solution was aerated with CO gas at an inlet flow rate of 8.2 mL/min. There is a noticeable plasmon shift as a function of increased seed concentration. The seed concentrations were 200, 300, 350, and 400uL that resulted in SPR peak positions of 508, 517, 537, and 540nm respectively.

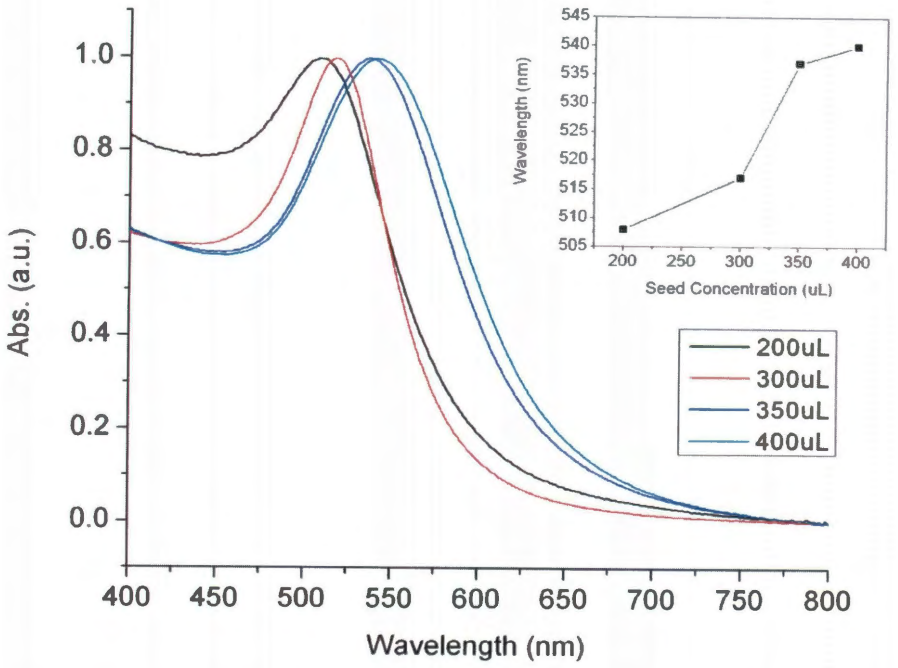

Figure 8.4. Normalized UV-visible spectra of Au colloid synthesized by carbon monoxide gas with addition of seed particles. The seed concentrations were 200uL, 300uL, 350uL, and 400uL. The inset plots the SPR peak position of the Au colloid vs. seed concentration. The SPR peek positions were 508, 517, 537, and 540nm corresponding to seed concentrations of 200, 300, 350, and 400uL.

The results seem counter intuitive since one would assume a lower seed concentration would result in a lack of nucleating sites for the reduction of the free $[AuCl_4]^-$ ions in solution leading to lager shell growth. One would also assume that a blue-shift would be present as the seed concentration increased from 200uL to 400uL since the number of available reducing particles increased. However we observe the opposite effect. This can be explained due to the nature of the CO reduction. Since the CO gas is introduced into the aqueous solution at a rate of 8.2 mL/min a higher seed concentration is necessary to ensure that there has ample surface area for the $[AuCl_4]^-$ ions to reduce to before new nuclei are formed in the solution. At a seed concentration of 200uL there are not enough particles of sufficient size to prevent a new induction period of nucleation growth from occurring. At the higher seed concentrations the reduction sites are sufficient to prevent

new nuclei from forming. Increasing the gas injection flow rate higher than 8.2 mL/min caused an increase in second-generation nuclei formation that reduced the overall particle size diameter that broadened and blue-shifted the SPR peak.

Chapter 9: Au Nanoparticle Surface Modifications

9.1 Au colloid surface functionalization

The surfaces of nanoparticles can be easily functionalized with various organic and bimolecular ligands, among which the molecules with a sulfur head group. The strong affinity of sulfur to gold has been exploited to form molecular contacts, to link other specious to the gold surface, or to form well-ordered self assembled monolayers (SAMs). Recent strategies have employed thiol capped DNA oligonucleotides to link gold nanoparticle building blocks to form periodic functional assemblies, in addition to serving as efficient DNA detection schemes.

Gold nanoparticles (25 $\pm$ 2nm) were prepared by carbon monoxide reduction of chloroauric acid. A sparse self-assembled monolayer (SAM) of thiolated ss-DNA was formed on the surface of the gold nanoparticles by incubating purified DNA, 25bp in length, with 1mL of nanoparticles at room temperature for 24 hours. The nanoparticle concentration, per sample, remained constant while the DNA concentration ranged from 200pmol to 1000pmol in increments of 100pmol. The nanoparticle-DNA conjugates were allowed to precipitate and the supernatant removed. This precipitation step was conducted three times before the nanoparticles were characterized. The DNA/nanoparticle conjugates remained stable at room temperature for several months. The extinction spectra (400-800nm) of thiolated DNA –modified nanoparticles and unmodified gold nanoparticles are shown in Figure 9.1.

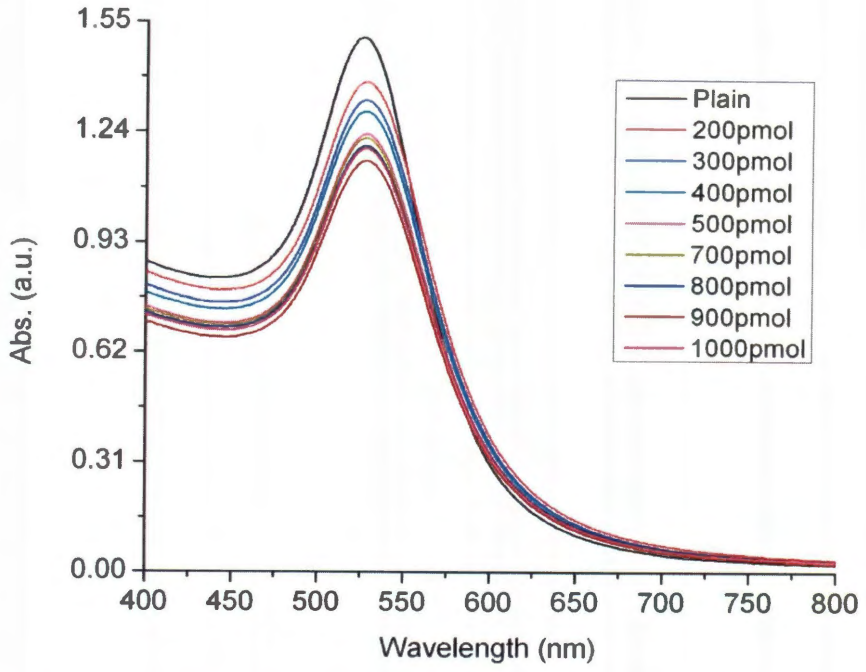

Figure 9.1. UV-visible extinction spectrum of unmodified ~25nm AuNPs (black) and DNA-modified AuNPs at various incubation concentrations of purified DNA in the wavelength range of 400-800nm.

As evidenced by the spectra, the gradual formation of a SAM of thiolated DNA on the gold nanoparticle surface by gold-sulfur bonding caused a shift in the surface plasmon absorption peak from 526 to 530nm.

9.2 SPR response to particle surface interface changes

Surface plasmon absorption properties are generally discussed within the framework of the Drude model [36] according to which the plasmon peak position ($\lambda_{sp\,max}$) depends on the dielectric constant surrounding the medium (ϵ_m), as governed by

$$\lambda_{sp\,max}{}^2 = \lambda_p{}^2(\epsilon_\infty + 2\epsilon_m) \ , \tag{30}$$

where $\epsilon_\infty$is the high-frequency dielectric constant of gold due to the interband and core transitions. λ_p is the bulk plasmon frequency of gold given by the following relation:

$$\lambda_p = \frac{2\pi c}{\left(\frac{Ne^2}{m_e \epsilon_0}\right)^{\frac{1}{2}}} \quad , \tag{31}$$

where ϵ_0 is the permittivity of free space in a vacuum, c is the speed of light in a vacuum, e is the electronic charge, N is the density of free electrons in the nanoparticle, and m_e is the effective mass of the electron. The red shift in the plasmon wavelength resulting from the formation of the SAM can thus be attributed to a local increase in the medium refractive index as a result of the thiols or to a change in the free electron density of the gold nanoparticle due to the strong surface coupling with sulfur [14]. The SAM formation also leads to an observable broadening of the plasmon band of the nanoparticles, as attributed commonly to chemical interface damping [35].

Chapter 10: Summary

In summary we have reported a facile and size-controlled synthesis of monodispersed gold nanoparticles utilizing carbon monoxide as a reducing agent. The resultant nanoparticles were stable in water at room temperature for up to 6 months. It was shown via statistical analysis that the average standard deviation of the nanoparticles fell within 11%. The resulting nanoparticle sizes can be tuned to a certain degree by varying the gas injection flow rate and chloroauric acid concentration.

Moreover, the effect of speciation on nanoparticle synthesis and particle properties was investigated. It was demonstrated that gold hydrolysis greatly affects nanoparticle size and monodispersity. Aging of the gold hydroxide solution prior to synthesis manipulates the availability of certain $[AuCl_x(OH)_{4-x}]$ species. Exploiting the control of $[AuCl_x(OH)_{4-x}]$ species development, by addition of K_2CO_3 and aging of the solution, Au colloid in the ranges of 15 to 80nm in diameter were produced.

Mie theory clearly illustrates the size dependent optical nature of the nanoparticles. Additionally, surface functionalization results in a change in the optical response of the nanoparticle surface plasmon and is described via the Drude model. Future work will explore the effects of solution temperature prior to CO gas reduction. Preliminary results show that solution temperature affects the final morphology of the AuNPs. Cell cytotoxicity studies comparing CO-AuNPs vs citrate based AuNPs will be also be explored.

References

[1] C. Shan, F. Li, F. Yaun, G. Yang, L. Niu and Q. Zhang, "Size-controlled synthesis of monodispersed gold nanoparticles stabilized by polyelectrolyte-functionalized ionic liquid," Nanotechnology **19** (28), 285601 (2008).

[2] J. K. Beattie, "Monodispersed colloids of transition metal and lanthanide compounds," Pure and Applied Chemistry **61** (5), 937-941 (1989).

[3] J. Turkevich, P. C. Stevenson, and J. Hillier, "The formation of colloidal gold," Volume 57, 1953

[4] D. G. Duff and A. Baiker, "A new hydrosol of gold clusters. Formation and particle size variation," Langmuir **9**, 2301-2309 (1993).

[5] S. Link and M. A. El-Sayed, "Size and temperature dependence of the plasmon absorption of colloidal gold nanoparticles," J. Phys. Chem. B **103**, 4212-4217 (1999).

[6] B. E. Brinson, J. B. Lassiter, C. S. Levin, R. Bardhan, N. Mirin, and N. J. Halas, "Nanoshells Made Easy: Improving Au Layer Growth on Nanoparticles Surfaces," Langmuir **24**, 14166-14171 (2008).

[7] J. Hu, Z. Wang, and J. Li, "Gold nanoparticles with special shapes: controlled synthesis, surface-enhanced raman scattering, and the application in biodetection," Sensors **7**, 3299-3311 (2007).

[8] S. Park, M. Park, P. Han, and S. Lee "The effect of pH-adjusted gold colloids on the formation of gold clusters over APTMS-coated silica cores," Bull. Korean Chem. Soc **27** (9), 1341 (2006).

[9] J. Polte, r. Erler, F. Emmerling, and R. Kraehnert, "Nucleation and growth of gold nanoparticles studied via in situ small angle X-ray scattering at millisecond time resolution," ACS Nano **4** (2), 1076-1082 (2010)

[10] H. Hovel, S. Fritz, A. Hilger, and U. Kreibig, " Width of cluster plasmon resonances: Bulk dielectric functions and chemical interface damping," Physical Review B **48** (24) "(1993).

[11] I. Srnova and B. Vlckova, "Two-dimensional assembling of Au nanoparticles mediated by tetrapyridylporphine molecules," Nano Letters **2** (2), 121-125 (2002).

[12] J. Turkevich, "Colloidal gold. Part I historical and preparative aspects, morphology and structure," Gold Bull. **18**, 3 (1985).

[13] F. Xiaotai, W. Zhenping, and L. Shuangfang, "Mechanisms and solubility equations of gas dissolving in water," Science in China B **39** (5) (1996).

[14] P. K. Jain, W. Qian, and M. A. El-Sayed, "Ultrafast cooling of photoexcited electrons in gold nanoparticle-thiolated DNA conjugates involves the dissociation of the gold-thiol bond," J. Am. Chem. Soc. **128** (7), 2426-2433 (2006).

[15] C. S. Barton, L. Waniganayake, G. Wei, and L Wieczorek, "Functional monolayer surfaces on gold nanoparticles for specific binding of histidine-tagged proteins," ICONN **6**, (2006).

[16] C. Yeh, C. Hung, and Y.C. Lin, "An immunoassay using antibody-gold nanoparticle conjugate, silver enhancement and flatbed scanner," Microfluid Nanofluid **6**, 85-91 (2009).

[17] W. Yang, J. Wang, S. Zhao, and C. Sun, "Multilayered construction of glucose oxidase and gold nanoparticles on Au electrodes based on layer-by-layer covalent attachment," Electrochemistry communications **8**, 665-672 (2006).

[18] Z. Wu, G. Zhou, and R. Q. Yu,"Gold colloid-bienzyme conjugates for glucose detection utilizing surface-enhanced raman scattering," Talanta **70**, 533-539 (2006).

[19] T. Sakai and P. Alexandridis, "Size and shape-controlled synthesis of colloidal gold through autoreduction of the auric cation by poly(ethylene oxide)-poly(propulene oxide) block copolymers in aqueous solutions at ambient conditions," Nanotechnology **16**, S344-S353 (2005).

[20] C. Lemire, R. Meyer, and H. J. Freund, "Do quantum size effects control CO adsorption on gold nanoparticles ?," Surface Chemistry Angew. Chem. Int. Ed. **43**, 118-121 (2004).

[21] B. Bahrami, A. Khodadadi, M. Kazemeini, Y. Mortazavi, "Enhanced CO sensitivity and selectivity of gold nanoparticles-doped SnO_2 sensor in presence of propane and methane," Sensors and Actuators B: Chemicals **133**, 352-356 (2008).

[22] S. Wang, K. Qian, X. Bi, and W. Huang, "Influence of speciation of aqueous $HAuCl_4$ on the synthesis, structure, and property of Au colloids," J. Phys. Chem. C **113**, 6505-6510 (2009).

[23] H. G. Hertz, "Structure of the salvation shell of dissolved particles," Angew. Chem. Internat. Edit. **9** (2) (1970).

[24] U. J. Jauregui-Haza, E. J. Fontdevila, and H. Delmas, "Solubility of hydrogen and carbon monoxide in water and some organic solvents," Latin American Applied Research **34**, 71-74 (2004).

[25] P. Scharlin, R. Battino, E. Silla, I. Tunon, and J. L. Ahuir, "Solubility of gases in water: correlation between solubility and the number of water molecules in the first salvation shell," Pure and Applied. Chem. **70** (10), 1895-1904 (1998).

[26] S. Dou, S. Chengquan, and Z. Yuenian, "Advances in Aquo-compound of natural gas," Lanzhou: Lanzhou University Press, 1992.

[27] L. Chengyuan, "Experiments of physical chemistry, Beijing: People's Education Press, 330, (1980).

[28] T. F. Jaramillo, S. H. Baeck, E. W. McFarland, "Catalytic activity of supported Au nanoparticles deposited from block copolymer micelles," J. Am. Chem. Soc. **125**, 7148-7149

[29] N. R. Jana, L. Gearheart, and C. J. Murphy, "Seeding growth for size control of 5-40nm diameter gold nanoparticles," Langmuir **17**, 6782-6786 (2001).

[30] L. Bickford, R. Drezek, and T. K. Yu, "Silica-gold nanoshells as potential intraoperative molecular probes for HER2-overexpression in ex vivo breast tissue using near-infrared reflectance confocal microscopy," *Breast Cancer Research and Treatment.* Online first (2009).

[31] R. C. Jin, Y. W. Cao, J .G. Zheng, "Photoinduced conversion of silver nanospheres to nanoprisms," Science **294**, 1901-1903 (2001).

[32] L. Yu, I. A. Banerjee, and H. Matsu, "Direct growth of shaped-controlled nanocrystals on nanotubes via bilological recognition," J. Am. Chem. Soc. **125**, 14837-14840 (2003).

[33] A. P. F. Turner, "Biosensors-sense and sensitivity," Science **290**, 1315-1317 (2000).

[34] C. Destree and J. B. Nagy, "Mechanism of formation of inorganic and organic nanoparticles from microemulsions," Advances in Colloid and Interface Science 123-126 (2006).

[35] B.N.J. Persson, Surface Science **281**, 153 (1993).

[36] P. Mulvaney, "Surface plasmon spectroscopy of nanosized metal particles," Langmuir **12**, 788-800 (1996).

Appendix A: Particle Analysis Using WCIF ImageJ Collection

ImageJ is a public domain Java image processing program inspired by NIH Image for the Macintosh. It runs on any computer with a Java 1.1 or later virtual machine, either as an online applet or as a downloadable application. The best source of information about ImageJ can be found at the ImageJ homepage (http://rsb.info.nih.gov/ij/). This appendix is meant to be an introduction to ImageJ for particle analysis and counting – a small part of ImageJ's repertoire. ImageJ has a large number of native functions supplemented by an ever increasing number of "plugins". The core functions are described in detail on the ImageJ web site (follow the Documentations link). A plugin is a file (named *.class) which needs to be in the "plugins" sub-folder of the ImageJ folder, otherwise ImageJ will not load it.

1 Installing ImageJ

If you already have ImageJ installed, it may be worthwhile uninstalling it (rename the folder) and following the installation instructions below. This will match your copy of ImageJ to this manual. Extra plugins can be easily added later.

1.1 Install program files

1. Download the WCIF_Imagej_setup.exe file from the Wright Cell Imaging Facility's website (http://www.uhnresearch.ca/wcif). Follow the Downloads link.

2. Run the program.

3. A shortcut will be installed on your desktop and in your Start menu.

1.2 Update core program

Now upgrade the ImageJ core program (file IJ.JAR) immediately from the ImageJ web site (See Section 1.5.1 below) – due to the frequency of upgrades, the version in the setup will be out of date.

1.3 Set memory allocation

Unlike other Windows applications ImageJ will only use the memory allocated to it. By default the WCIF ImageJ installation assumes a PC with 512Mb RAM, so ImageJ has been allocated 380 Mb by default (a recommended 75% of the total 512Mb). If your PC does not have 512Mb of RAM then change the allocated memory to equal 75% of total RAM via the menu commands: "Edit/Options/Memory". Specifying more than 75% of real RAM results in virtual RAM being used causing ImageJ to become very slow and unstable. See http://rsb.info.nih.gov/ij/docs/install/.

2 Upgrading

2.1 ImageJ core program

You do not need to be logged in as an administrator to do this, but ImageJ must be closed. ImageJ upgrades are very frequent, and major bugs addressed within days so ImageJ itself should be upgraded routinely. You can check your version of ImageJ by either noting the version that appears below the toolbar at start up, or by finding the version at the bottom of the ImageJ property list which can be called via the menu

command "Plugins/Utilities/ImageJ properties...". The latest version of ImageJ is available at: http://rsb.info.nih.gov/ij/upgrade/.

The file needed is called IJ.JAR. Download the new IJ.JAR to the "C:\ImageJ" directory and over-write the existing IJ.JAR. Upgrades are currently being released almost on a weekly basis. Details of the upgrade features can be found on the News page link on the ImageJ homepage site.

2.2 Plugins

The ImageJ/News page also has details about new plugins. These *.class files need to be downloaded to "C:\ImageJ\plugins". ImageJ will load all the plugins in the plugins folder at start up. Plugins saved to the plugins folder after ImageJ will not be available until ImageJ has been restarted. Other plugins can be found on the ImageJ/Plugins web-page.

3 Importing image files

ImageJ primarily uses TIFF as the image file format. The menu command "File/Save" will save in TIFF format. The menu command "File/Open" will open TIFF files and import a number of other common file formats (e.g. JPEG, GIF, BMP, PGM, PNG). These natively supported files can also be opened by drag-and-dropping the file on to the ImageJ toolbar. Several more file formats can be imported via ImageJ plugins (e.g. Biorad, Noran, Zeiss, Leica). When you subsequently save these files within ImageJ they will no longer be in their native format. Bear this in mind; ensure you do not overwrite original data. There are further file formats such as PNG, PSD (Photoshop),

ICO (Windows icon), PICT, which can be imported via the menu command "File/Import/Jimi Reader…".

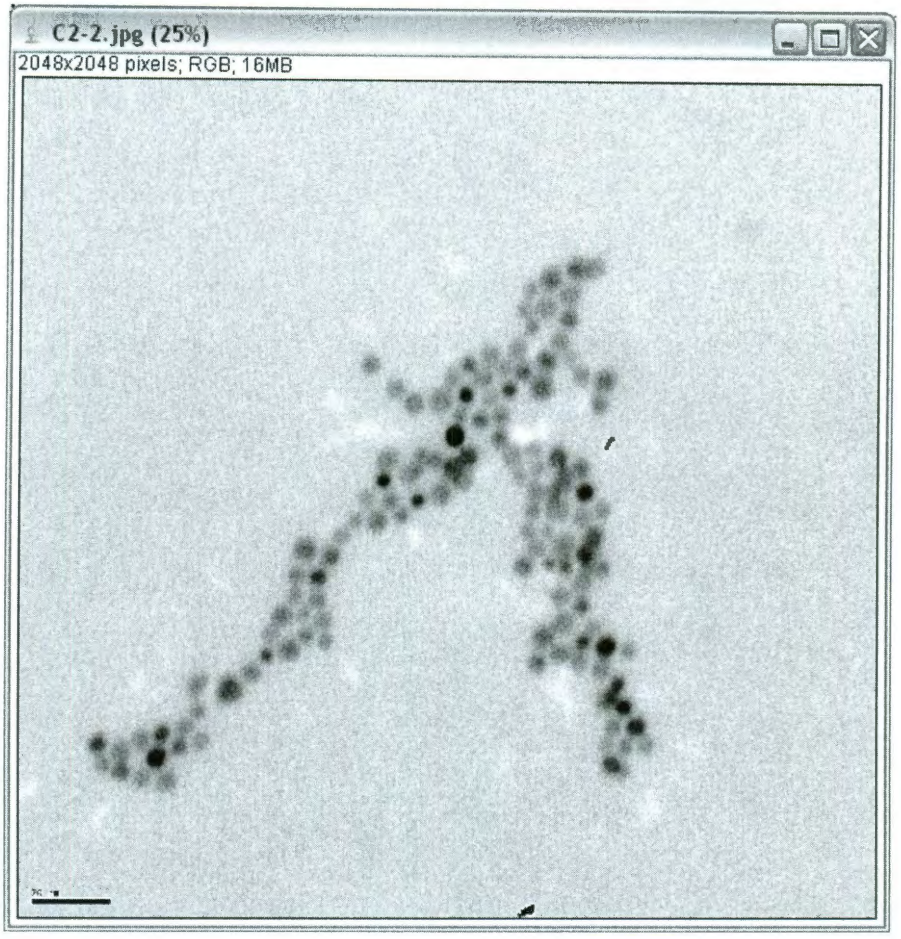

Figure A1. Imported TEM image of gold nanoparticles in ImageJ.

4 Particle analysis

Particle counting can be done automatically if the specimen lends itself to it, i.e. the individual particles can touch – but not too much! If automatic particle counting cannot be done, ImageJ can facilitate manual counting with the "Point Picker" or "Cell counter" plugin.

4.1 Set scale bar

To set the scale bar for particle measurements select the "straight line" icon in the ImageJ toolbar.

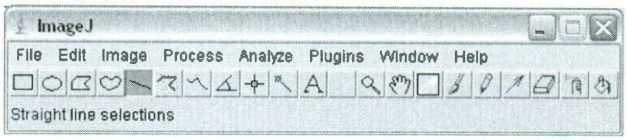

Figure A2. ImageJ toolbar "straight line" selection.

Next measure the length of the imbedded toolbar in the image. Afterwards select "Analyze - Set Scale". A dialog box will appear. Input the known distance and set unit of length to nanometers.

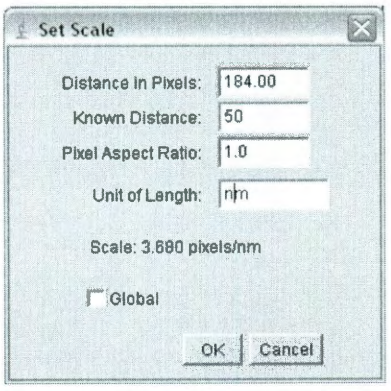

Figure A3. Set scale dialog box.

After setting the scale the original scale bar in the image needs to be removed. Select the "Rectangular" selection icon in the toolbar and enclose the scale bar in the image. Next

select "Edit – Clear". The area contained within the rectangle will be cleared. Next select "Edit – Fill" to make the area white.

4.2 Threshold segmentation

Automatic particle analysis requires the image to be a "binary" image i.e. black or white. The software needs to know exactly where the edges are to perform morphology measurements. A "threshold" range is set and pixels in the image whose value lies in this range are converted to black; pixels with values outside this range are converted to white (or vice-versa depending on what the user requests). There are several ways to set thresholds. Select "Process – Binary – Threshold" to generate a black and white binary image.

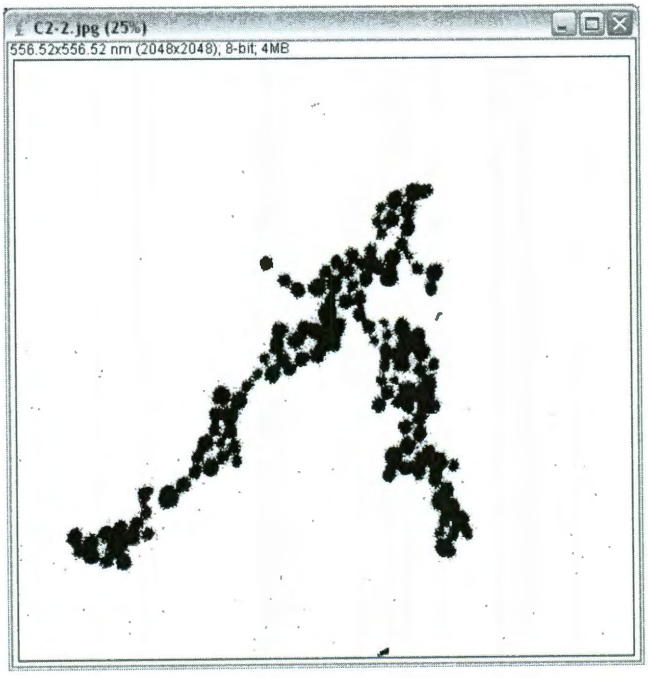

Figure A4. Binary image conversion.

4.3 Watershed segmentation

Objects in a binary image that are slightly overlapping may be separated using the menu command "Process/Binary/Watershed". The image first needs to be converted to binary (set via thresholding). The black pixels are then replaced with grey pixels of an intensity proportional to their distance from a white pixel (i.e. black pixels close to the edge are light grey, those closer to the 'middle) are nearer black. This is the Euclidian distance map (EDM). From this it calculated the centers of the objects the ultimate eroded points (UEPs), i.e. points that are equidistance from the edges. These points are then dilated until the meet another black pixel, and then a watershed line is drawn.

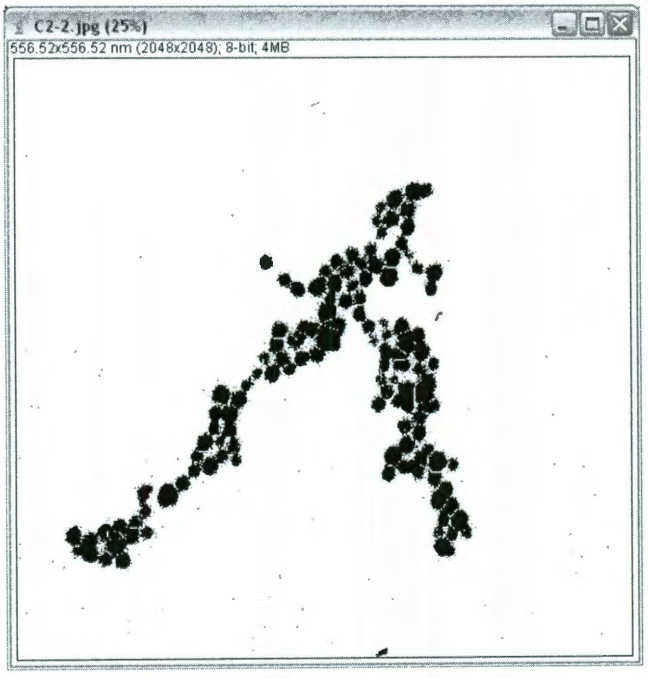

Figure A5. Watershed segmentation of binary image.

4.4 Analyze Particles

Once the image has been segmented, the menu command "Analyze - Analyze Particles" can be used to obtain various information regarding particle size and numbers. Set the minimum size and maximum size to exclude objects that appear in the binary image that are clearly not objects of interest. Select the "Show: Outlines", "Display Results", and "Summarize" options to display an image of the detected objects, a box containing results, and a box containing a summary. The summary box will contain the nanoparticle count, area, and average particle size.

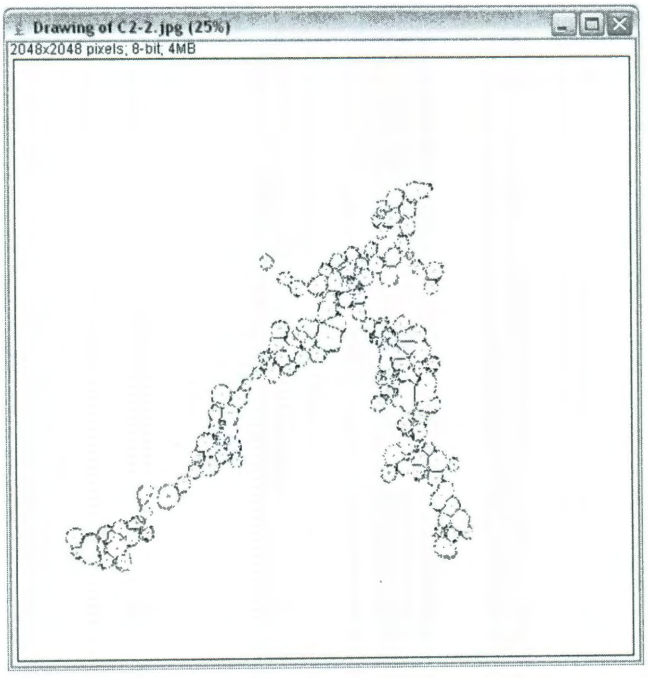

Figure A6. Particle analysis outline.

4.5 Particle Histogram

To generate a histogram and standard deviation select "Analysis – Distribution" a distribution dialog box will appear. Set the bin size to 20% of the total particle count. Set

the range from the smallest know particle to the largest. A histogram will be generated containing statistical data.

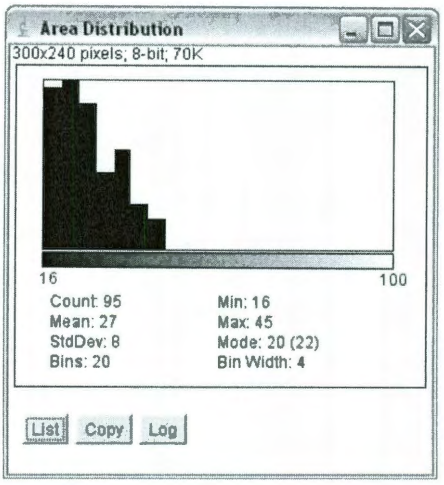

Figure A7. Nanoparticle histogram of TEM image.

The particle analysis can be automated via plugins or macros once the correct threshold value and particle size range has been determined for your objects of interest.

Appendix B: Thermodynamics of $HAuCl_4$ Reduction

The entire process is performed between 20 and 22°C and a pressure of 1 atm. The pH of the solution varies as a function of $HAuCl_4$ concentration. Nernst equation describes potential of electrochemical cell as a function of concentrations of ions taking part in the reaction:

$$E = E^0 - \frac{RT}{nF}\ln(Q) \tag{32}$$

where E^0 is the standard reduction potential, R is the absolute gas constant = 8.31441 J/(mol K), F is Faraday constant = 96484.6 C/mol, T is the absolute temperature = 295.15 K, n is number or electrons, and Q is the reaction quotient. RT/F can be considered constant.

$$Q = \frac{\{C\}^c\{D\}^d}{\{A\}^a\{B\}^b} \tag{33}$$

$$E = E^0 - \frac{RT}{nF} * 2.303 * \log(Q) \tag{34}$$

The CO gas is injected at a flow rate of 25.45 mL/min in 40 mL aqueous sample volumes. A water saturation constant of 0.26 g per 1 kg at 22°C is used.

$$Au^{3+} + 2e^- \rightarrow Au^0 \quad E^0(V) = 1.52 \tag{35}$$

$$AuCl_4^- + 2e^- \rightarrow AuCl_2^- + 2Cl^- \quad E^0(V) = 0.926 \tag{36}$$

$$AuCl_2^- + e^- \rightarrow Au^0 + 2Cl^- \quad E^0(V) = 1.154 \tag{37}$$

$$AuCl_4^- + 3e^- \rightarrow Au^0 + 4Cl^- \quad E^0(V) = 1.002 \tag{38}$$

$$CO(g) + H_2O \rightarrow CO_2(aq) + 2e^- + 2H^+ \quad E^0(V) = 0.11 \tag{39}$$

$$CO(g) + 2H_2O \rightarrow HCO_3^- + 2e^- + 3H^+ \quad E^0(V) = -0.101 \qquad (40)$$

Redox potentials (39) and (40) are given at pH 0. The redox potentials are pH-dependent and must be adjusted for the varying pH values. The pH increase is dependent on $HAuCl_4$ concentrations and the CO saturation constants versus water are compensated for. The redox potentials for equations (39) and (40) are shown in Table B.1.

Table B.1. Reduction potentials for CO gas as a function of pH

$CO(g) + H_2O \rightarrow CO_2(aq) + 2e^- + 2H^+$		$CO(g) + 2H_2O \rightarrow HCO_3^- + 2e^- + 3H^+$	
pH	Redox potential (V)	pH	Redox potential (V)
3.25	0.300	3.25	0.089
3.6	0.321	3.6	0.110
3.79	0.332	3.79	0.121
4.05	0.347	4.05	0.136
4.25	0.359	4.25	0.148
5.55	0.435	5.55	0.224
6.6	0.496	6.6	0.285
7.45	0.546	7.45	0.335
8.8	0.625	8.8	0.414
9.23	0.650	9.23	0.439
10.3	0.713	10.3	0.502
11.4	0.777	11.4	0.566